A study of charged particle emission from the β-decay of ^{8}He

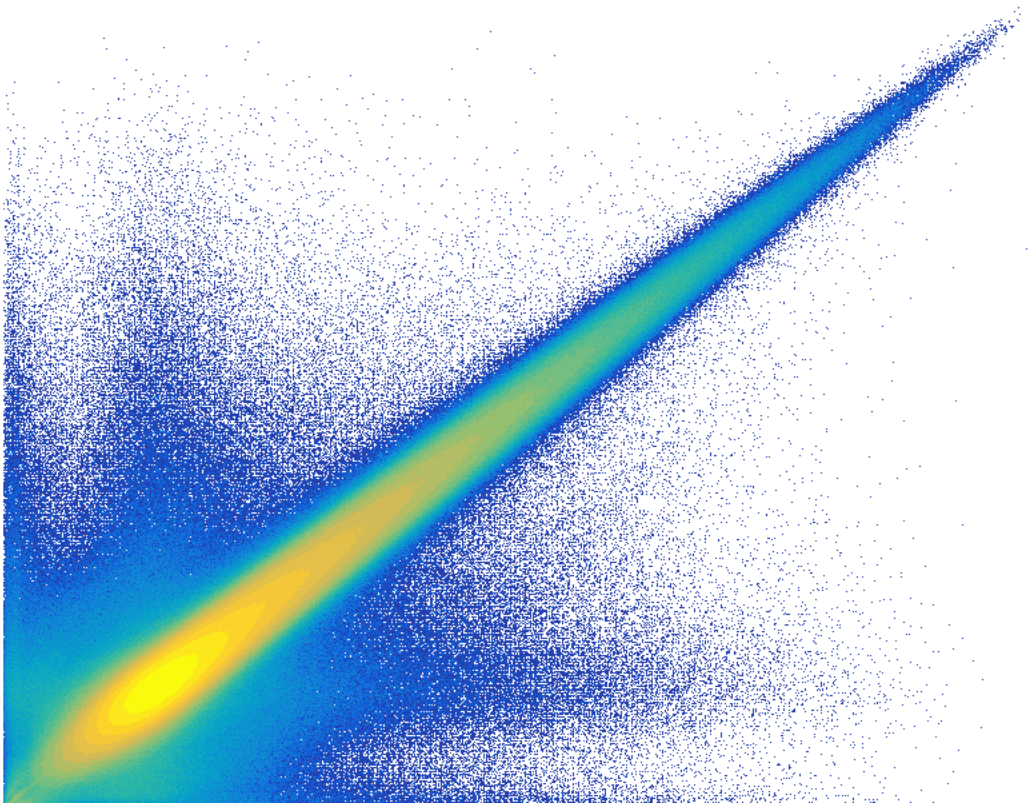

Christiane Rahbek
201804946

Master's Thesis in Physics
June 2023

Supervisor: Hans O. U. Fynbo
Department of Physics and Astronomy
Aarhus University

Colophon

A Study of Charged Particle Emission from the β-Decay of ^{8}He

— En undersøgelse af ladede partikler udsendt fra betahenfaldet af ^{8}He

Master's thesis by Christiane Rahbek. Written under supervision by Hans O. U. Fynbo, Department of Physics and Astronomy, Aarhus University.

Typeset by the author with LaTeX and the memoir document class, using Linux Libertine and Linux Biolinum 11.0/13.6pt.

Printed at Aarhus University

Abstract

This thesis aims to investigate the β-delayed charged particle emission from ^{8}He through the decay $^{8}\text{He} \rightarrow {}^{8}\text{Li}^{*} \rightarrow \alpha + \text{t} + \text{n}$. This is done by measuring the decay of ^{8}He, produced at the ISOLDE facility at CERN, and finding αt-coincidences with double-sided silicon strip detectors. The experiment does however, induce a background of $\alpha\alpha$-coincidences from another decay branch of ^{8}Li. Therefore, the focus of much of this work is on how to remove this background when we only look at measurements of charged particles. In order to remove $\alpha\alpha$-coincidences a lot of data with possible αt-coincidences was removed. Therefore, a lower boundary of the branching ratio of the αtn-decay branch is found to be $(0.174 \pm 0.0023)\%$. To get a more precise value of the branching ratio, I propose that we need to include neutron coincidences into the analysis, as well as doing a time calibration on all the detectors to ensure that data measured in different strips and detectors is compared correctly.

Acknowledgements

This thesis concludes my Master's degree in Physics at Aarhus University. I would therefore like to thank my supervisor Hans O. U. Fynbo for his supervision first during my Bachelor's project and now during my Master's thesis. Your door has always been open and I appreciate your willingness to help me and guide me through my problems. It has provided me with much academic growth.

I would furthermore like to thank the rest of the Aarhus University Subatomic Group for your help and support as well. I have enjoyed being part of such supportive and constructive work environment where I have always felt seen, heard and cabable of solving my problems. I would like to give a big thanks to Erik A. M. Jensen for being willing to spend hours troubleshooting my code, helping me in the Linux terminal, and listening to me when things did not go my way. Furthermore, I would like to send my gratitude towards Karsten Riisager for his valuable insight and willingness to share from his experience.

I would also like to thank my office mates during this past year for their support. We have laughed, been distracted and helped each other. It has made the office a nice working environment.

Finally, I would like to thank Erik and my family and for their love and support.

Christiane Rahbek
Aarhus University, June 2023

Contents

Chapter 1

Introduction

In pysics we use the Standard Model to describe three out of the four fundamental forces of physics. The Standard Model has been very successfully predicting several different fundamental particles, such as the top quark [1, 2] and the Higgs Boson [3, 4]. However, the Standard Model fall short in several aspects of Physics. As an example, it does not yet have a consistent way to describe the masses of neutrinos [5]. We therefore need to improve it or make a new model. To make a better model we therefore need more knowledge about the properties of neutrinos. This is among other experiments done in neutrino reactors. In neutrino reactor experiments the inverse β-decay is observed

$$\bar{\nu}_e + p \rightarrow e^+ + n \tag{1.1}$$

where the positron and the neutron is measured and can be used to determine the energy of the neutrino [6].

In these experiments, some of the neutrons measured come from radioactive isotopes produced by cosmic rays. The energy spectrum of these neutrons cause a background in the experiment, which we will be able to remove if we have a detailed knowledge of their decay scheme. Some of the most important types of background of this type is ^{8}He and ^{9}Li [6, 7], which can produce β-delayed neutrons. It is therefore crucial to have a good understanding of the decay schemes of ^{8}He and ^{9}Li.

1.1 The Aim and Structure of this Thesis

In this thesis I will be investigating the β-delayed particle emission of

$$^8\mathrm{He} \rightarrow {}^8\mathrm{Li}^* \rightarrow \alpha + \mathrm{t} + \mathrm{n} \tag{1.2}$$

to get a better understanding of the branching ratios and energies of the neutrons produced by this decay. To do so I will be analyzing data from the decay of ^{8}He taken at CERN-ISOLDE in May 2022. The decay scheme of ^{8}He is not known well enough, which we hope to improve with this experiment. The decay scheme of ^{8}He as it is known now, can be seen in fig. 1.1. Several experiments have been conducted

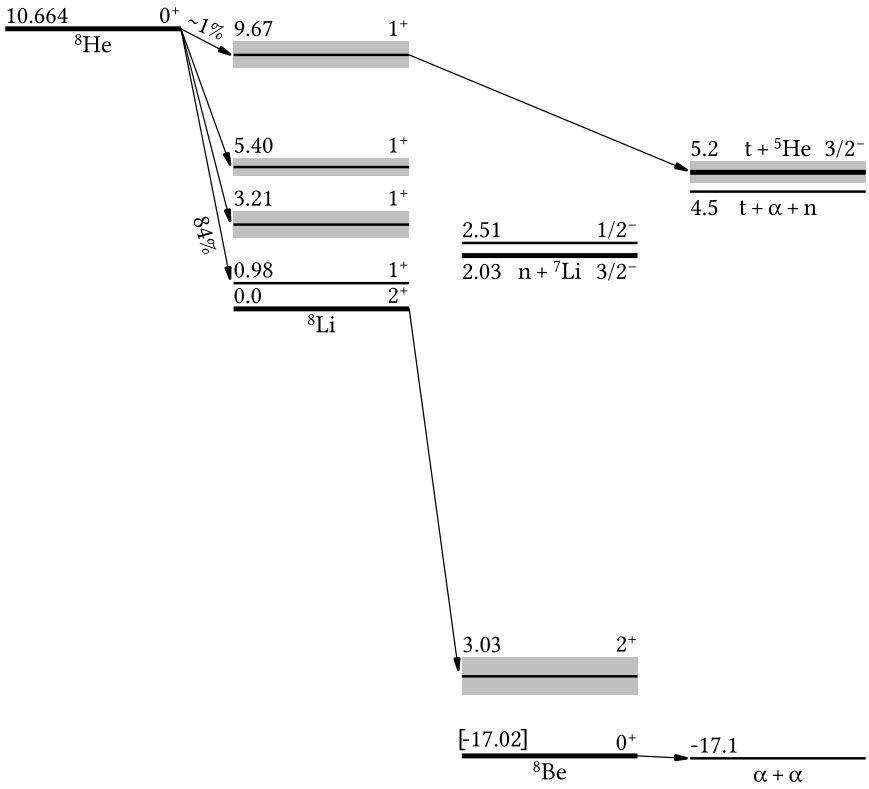

FIGURE 1.1: Decay scheme of ^{8}He.

with the purpose of getting a better understanding of the decay scheme of ^{8}He [8, 9, 10]. Additional analysis methods on these data have also been used [11, 12]. Even though all of these attempts have been made, there is no conclusive agreement on the branching ratios of the different excited states in ^{8}Li or on the exact energy of what is marked as the 9.67 MeV excited state of ^{8}Li in fig. 1.1. As we can see the only possible ways for the decay in eq. (1.2) to happen is through either the 5.40 MeV or the 9.67 MeV states of ^{8}Li. There are not much knowledge about the branching ratios of the 5.40 MeV state of ^{8}Li, but an overview of the research of the 9.67 MeV state of ^{8}Li can be seen in table 1.1.

As it can be seen in table 1.1, there is no obvious agreement between experiments and methods about the energy of the 9.67 MeV state of ^{8}Li. A common factor in the earlier experiments is also the fact that not all the possible decay products from the decay of ^{8}He was measured. In the experimental setup for the data taken in this thesis, we have had the possibility to measure both the charged particles (α, t, β), the γ-rays, and the neutrons from the decay of ^{8}He. As we are able to measure all the particles in the decay, we should therefore have good conditions to get a better understanding of the decay of ^{8}He. To analyze all of this data is a complex and time consuming process, even if we only look at data relevant for the decay in eq. (1.2). Therefore, the goal for this thesis is to explore how much information we can extract about the decay in eq. (1.2) without doing the most time consuming parts of the work. This means that:

Ref.	Source of data	Analysis method	E_4 [MeV]	a_t [fm]	logft
[8]	Measures β-γ and β-n coincidences	Fit to double Brieght-Wigner shape accounted for neutron broadning	–	–	–
[9]	Measures tritons	Fit to triple Breit-Wigner shape	8.8	–	4.3
[11]	Analysis of data from [8, 9]	Four-level, eight-channel R-Matrix	9.06	4.6	3.14
[10]	Measures tritons	One-level, one-channel R-Matrix	9.3 ± 0.1	3.7	5.18
[12]	Analysis of data from [9]	Four-level, eight-channel R-Matrix	9.06	4.6	4.11
[12]	Analysis of data from [10]	Four-level, eight-channel R-Matrix	9.67	4.6	4.75
		One-level, one-channel R-Matrix	9.46	4.6	3.06
		One-level, one-channel R-Matrix	9.92	3.7	4.19

TABLE 1.1: Overview of current ^{8}He research. Only information about decays to the 9.67 MeV excited level in ^{8}Li has been included. E_4 is the energy of the 9.67 MeV excited level in ^{8}Li, and a_t is the channel radius, which is only used in R-matrix analysis, an analysis method I will not describe futhere here, but an overview can be found in [13]. The oldest research is in the top and the most recent is in the bottom. Be aware that the definition of logft is not consistent in all of the articles, and that the logft value is not directly comparable. This is possible as there is no unique definition for decay to a broad level [12] such as the 9.67 MeV state of ^{8}Li.

1. I will be looking for αt-coincidences only. Even though the neutrons from the decay have been measured, we will see how much information we can retrieve without searching for αtn-coincidences.

2. A time calibration between all the detectors in the setup will not be made. This means that not all detectors have measured the exact same times, and this will not be corrected. We will look further into this in chapter 6.

In this thesis we will also be looking at the β-delayed α-decay from ^{20}Na. This data will be used as a quality control of some of the methods used in this thesis as we will see in chapters 5 and 6. This thesis will therefore be structured as follows:

In chapter 2 I will introduce the theoretical framework for this thesis. Here I will talk about nuclear structure and different types of radioactive decay to get a better understanding of what happens through the different decay channels of ^{8}He and ^{20}Na.

In chapters 3 and 4 I will talk about how ^{8}He is produced at CERN, the experimental setup and what kind of data we end up measuring.

In chapter 5 I will begin to work with the measurements by applying and checking the quality of the calibration. Furthermore, I will be sorting through the data by a process called front/back-matching. In other words I will prepare the data for the data analysis presented in chapter 6.

In chapter 7 I will present the results found when using the methods i presented in chapter 6.

In chapter 8 I will discuss the results presented in chapter 7, discuss the methods I used in chapter 6 as well as suggesting some outlooks for further research.

Chapter 2

Theoretical Framework

The physics of nuclei can be described in many ways and ranges from few- to many-body dynamics and from classical to quantum mechanical descriptions [14]. All of this depends on what aspects of the nucleus we want to describe. Do we want to look at the nucleus as a single particle that interacts with other particles, or do we want to understand what holds the nucleus together? There are many possibilities. In nuclear physics we therefore have several different models that describe different aspects of the nucleus [14].

A commonly used model to describe the macroscopic properties of the nucleus is the liquid drop model, where the nucleus is regarded as a quantum liquid [14]. The semi-empirical mass formula which is used to describe the binding energy of a nucleus, arises from the liquid drop model, and is very successful close to the β-stability line [14]. We know that the nucleus is comprised of nucleons with an isospin projection of $\pm\frac{1}{2}$. These nucleons are more commonly known as protons and neutrons. If we on the other hand want to describe the interactions between nucleons in the nucleus, we have a many-body problem that we need to solve. A many-body problem is impossible to solve analytically, and is therefore not an ideal way to make a model for a nucleus. A successful description of these interactions is the shell model. The shell model is a mean field model that treats each nucleon as moving in a mean field generated by the other nucleons in the nucleus. A successful choice of mean field is the Woods-Saxon potential with a spin-orbit term [14], where clustered discrete single-particle energy levels will emerge. This creates the nuclear shells and correctly predicts the nuclear magic numbers given by:

$$2,\ 8,\ 20,\ 28,\ 50,\ 82,\ 126$$

The nuclear magic numbers give us the number of neutrons or protons needed in a nucleus to fill the outermost shell. Nuclei with filled shells are especially stable. Furthermore protons and neutrons tend to pair up so that they each have a total spin of 0 and and an even parity. This means that we would expect even-even nuclei to have a 0^+ ground state [14, 15].

2.1 Description of Radioactive Decays

There exist many possible configurations of the nucleons in the nucleus. Some of these configurations require more energy to hold the nucleus together than other. From these configurations, energy levels in the nucleus arises. When a nucleus undergoes radioactive decay the configuration of these nucleons will somehow change. Depending on the type of decay there exist different types of decay products, some of which we will cover in sections 2.1.1 and 2.1.2. The most general description of a nuclear decay is independent of the type of radioactive decay we are looking at. In the simplest case we are looking at a decay $A \to B$. We can then describe the number of nuclei in configuration A at the time t with the exponential decay law [15]:

$$N_A(t) = N_A(0)e^{-\lambda_A t} \tag{2.1}$$

Where $N_A(0)$ is the number of nuclei in configuration A at time $t = 0$ and λ_A is the decay constant of A, which is connected to the half-life of the nucleus by

$$t_{\frac{1}{2},A} = \frac{\ln(2)}{\lambda_A} \tag{2.2}$$

where $t_{\frac{1}{2},A}$ is the half-life of the nucleus in configuration A.

We do however, often have a case where the products of a radioactive decay are radioactive themselves. This results in a decay chain of the form $A \to B \to C$. So if we have a nucleus in configuration A that decays to a nucleus in configuration B at time t, then we can describe the number of nuclei in configuration B left at time t' with:

$$N_B(t, t') = \frac{\lambda_A}{\lambda_B - \lambda_A} N_A(t) \left[e^{-\lambda_A(t'-t)} - e^{-\lambda_B(t'-t)} \right] \tag{2.3}$$

Where λ_B is the decay constant of B. These equations are a result of the Bateman equations [16], and gives an understanding of how we would expect a radioactive decay to behave. Different kinds of radioactive decays do however, occur for different reasons and can be described with different physics. In this thesis we will be looking further at β-decays as well as different decays caused by barrier penetration.

2.1.1 β-Decays

β-decays are weak interactions induced by a change in the nuclear charge. We have two types of β-decay:

β^+-decays: A proton decays to a neutron

$$p \to n + e^+ + \nu_e$$

β^--decays: A neutron decays to a proton

$$n \to p + e^- + \bar{\nu}_e$$

In a β-decay the total number of nucleons in the nucleus stays the same, but as the ratio of protons to neutrons in the nucleus changes, the isospin projection of the nucleus will change as well. This means that we can use the isospin operators to describe β-decays. The most probable type of β-decay only induces a change in the isospin projection of our nucleus [14]. This is described with the Fermi operator:

$$F^{(\pm)} = \sum_{a=1}^{A} t_{\pm,a} \tag{2.4}$$

Where a indicates the a'th nucleon in the nucleus with A nucleons. This means that $t_{\pm,a}$ indicates a shift in the isospin of the a'th nucleon.

During a β-decay the nucleus can also have a change in its spin quantum number along with the change of isospin. This is less likely [14], but still happens. This process is described by the Gamow-Teller operator:

$$GT_i^{(\pm)} = \sum_{a=1}^{A} \sigma_{i,a} t_{\pm,a} \tag{2.5}$$

Where $t_{\pm,a}$ has the same meaning as before, and $\sigma_{i,a}$ indicates a spin change of i in the a'th nucleon in the nucleus. This means that i can be 0 or ± 1.

Selection Rules for β-decays

When nuclei undergoes β-decays they still need to obey the conservation laws of angular momentum. This helps us determine what transitions are allowed. This is what we call selection rules. In β-decays we have two selection rules that determines if a β-decay is allowed [17]:

One for the total spin

$$\vec{J}_i = \vec{J}_f + \vec{L} + \vec{S} \tag{2.6}$$

Where $\vec{J}_i$ is the total spin of the initial state, $\vec{J}_f$ is the total spin of the final state, $\vec{L}$ is the total angular momentum of the two leptons and $\vec{S}$ is the total spin of the two leptons.

And one for the parity

$$P_i = P_f(-1)^l \tag{2.7}$$

Where P_i is the parity of the initial state, P_f is the parity of the final state and l is the projection of the total angular momentum of the leptons.

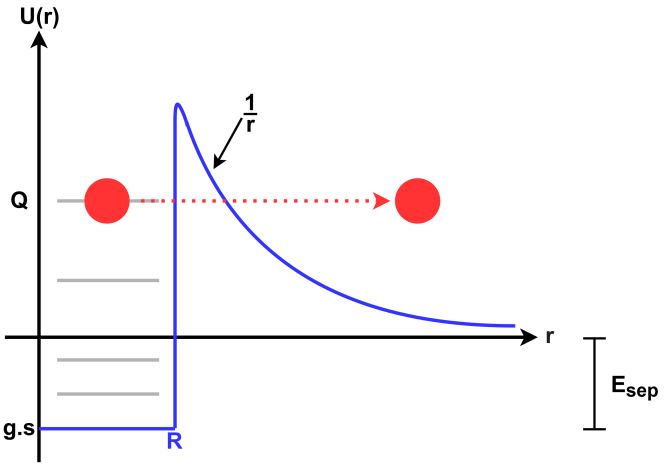

FIGURE 2.1: Illustration of barrier penetration. We can here see the potential energy of a system containing the daughter nucleus and the particle that will be emitted by the barrier penetration (marked by the red circle). The particle that will be emitted does not have enough energy to overcome the barrier. Instead it can tunnel through the barrier and thereby escape the mother nucleus. This will only be possible if the system is in a excited state that is higher than the separation energy E_{sep}.

2.1.2 Barrier Penetration

Radioactive decays caused by barrier penetration encompasses over several types of radioactive decay where α-decay is the most commonly-known. In this thesis we will be looking at three types of decay by barrier penetration: α-decay, triton emission and neutron emission. Common to all of them, a nucleus emits a particle which will release some energy, Q, from the reaction given by:

$$Q = E_M - E_D - E_P \tag{2.8}$$

Where E_M, E_D and E_P is the energy of the mother, daughter and emitted particle nucleus respectively. To understand decays by barrier penetration further, we have to understand how the nucleus is held together. Within a radius R of the nucleus, the nucleus is held together by a spherical potential caused by the nuclear force. If the nucleus lies in the bottom of the potential well, it is in its ground state. If the energy of the nucleus lies higher in the potential well, the nucleus is in an excited state. When we exceed the radius R, the repulsive Coulomb force becomes dominant. The Coulomb force experienced by the emitted particle is given by:

$$U(r) = \frac{Z_P Z_D e^2}{4\pi\epsilon_0 r} \tag{2.9}$$

Where Z_P and Z_D are the atomic numbers of the emitted particle end the daughter nucleus respectively, e is the electron charge, ϵ_0 is the vacuum permittivity and r is the distance from the center of the nucleus.

The process of barrier penetration is illustrated on fig. 2.1. As it can be seen, particles that decay through barrier penetration requires quantum tunneling through the

Coulomb barrier. Larger nuclei are more prone to undergo barrier penetration, as the Coulomb barrier is is lower at higher values of r. Furthermore nuclei in higher excited states have to penetrate a smaller barrier, and are therefore also more likely to decay by barrier penetration. This can be described by the penetrability, which is the probability that a particle will tunnel through the barrier, and thereby undergo some kind of radio active decay [17].

Selection Rules for Barrier Penetration Decays

The conservation laws of angular momentum and parity, must also be fulfilled by decays by barrier penetration. If we look at conservation of angular momentum we expect that

$$\vec{J_M} = \vec{J_D} + \vec{J_P} + \vec{L} \tag{2.10}$$

where $\vec{J_M}$, $\vec{J_D}$ and $\vec{J_P}$ are the orbital angular momentum of the mother, daughter and emitted particle nuclei respectively and $\vec{L}$ is the total angular momentum of the emitted nucleus-daughter system in the center of mass (CM).

If we look at the conservation rules for parity we would expect that

$$P_M = P_D P_P (-1)^l \tag{2.11}$$

where P_M, P_D and P_P are the parity of the mother, daughter and emitted particle nucleus respectively and l is the projection of the total angular momentum of the emitted nucleus-daughter system.

2.1.3 The Decay of ^{20}Na

In this thesis we will be looking at β-delayed α-decays from ^{20}Na. As we will see, we will need to convert the measured energies of the decay to an excitation energy. In this section I will through conservation of energy and momentum to find the excitation energy of the measured data. Let us first look at the reaction. ^{20}Na decays through:

$$^{20}\mathrm{Na} \rightarrow {}^{20}\mathrm{Ne}^{*} \rightarrow \alpha + {}^{16}\mathrm{O} \tag{2.12}$$

As we will see in chapter 4 we will be measuring the kinetic energy of the decay products which in this case will be ^{16}O and α. From conservation of momentum we know that

$$p_\alpha + p_O = \sqrt{2m_\alpha E_\alpha} + \sqrt{2m_O E_O} = 0 \tag{2.13}$$

where p_α, m_α and E_α are the momentum, mass and kinetic energy of the α-particle. p_O, m_O and E_O are the momentum, mass and kinetic energy of the ^{16}O nucleus. This will give us

$$E_\alpha = \frac{m_O}{m_\alpha} E_O \tag{2.14}$$

If we want to investigate the excitation energies of the compound nucleus ^{20}Ne, we then have to look at

$$E^*_{\mathrm{Ne}} = E_\alpha + E_O + E_{\alpha,\mathrm{sep}} = \left(\frac{m_O + m_\alpha}{m_O}\right) E_\alpha + E_{\alpha,\mathrm{sep}} \approx \frac{5}{4} E_\alpha + E_{\alpha,\mathrm{sep}} \tag{2.15}$$

where $E_{\alpha,\mathrm{sep}}$ is the separation energy of the α-particle from the compound nucleus. This means that we can find the excitation energies of our compound nucleus by measuring the the energy of the decay products α and ^{16}O.

2.2 Energy Loss in Materials due to Stopping Power

When a particle travels through a material it will loose energy depending on:

1. The distance travelled in the material.
2. What the incident particle is.
3. What material the particle travels through.

We can describe this loss of energy by the stopping power, which describes the energy loss of a particle as it travels through a material. The stopping power is defined as

$$S(E) = \frac{\delta E}{\delta L} \tag{2.16}$$

Where δE is the change in the energy of our particle while it travels through the length δL [18].

In this thesis I will be working with different projectiles that will be stopped in a carbon foil in the same experimental setup as we will see in chapter 4. These different projectiles will have different stopping powers in the carbon foil, and will therefore be stopped at different distances inside the foil. This will impact the energies we end up measuring, as we will discuss further in section 4.2.

Chapter 3

The ISOLDE Facility at CERN

The experiment for this thesis has been conducted at the ISOLDE facility at CERN. ISOLDE specializes in accelerating beams of exotic nuclei for nuclear physics studies and is part of the large accelerator network at CERN, which can be seen on Figure 3.1.

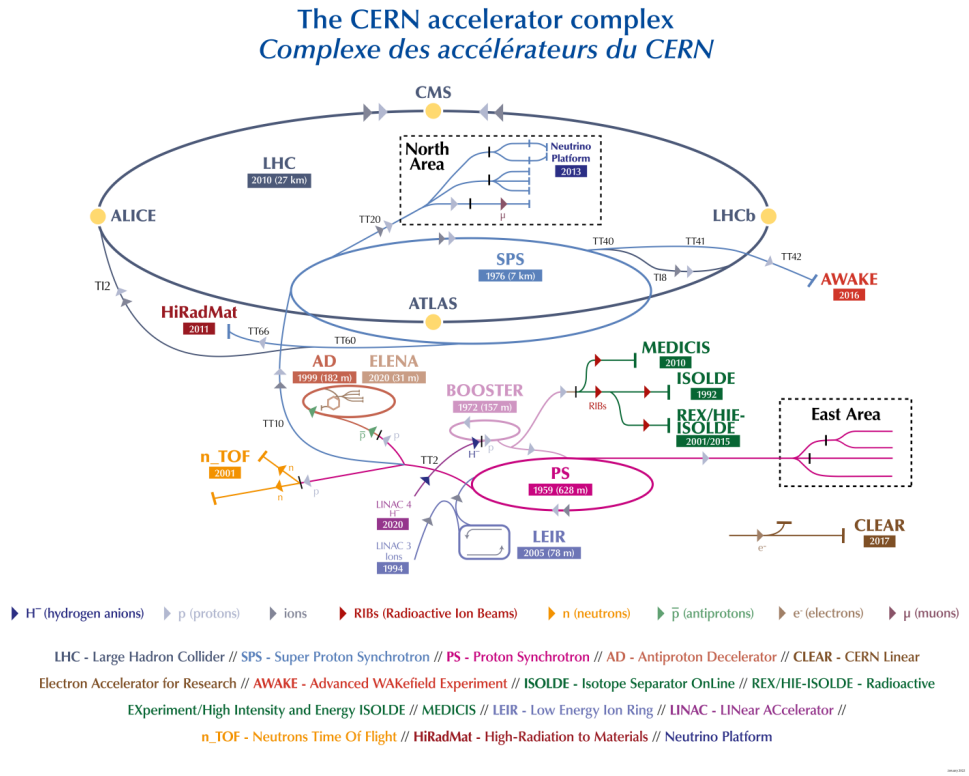

Figure 3.1: The accelerator complex at CERN in January 2022 from [19].

ISOLDE receives accelerated protons from the PS-BOOSTER, which also provides protons to other accelerators at CERN such as the LHC. The protons from the

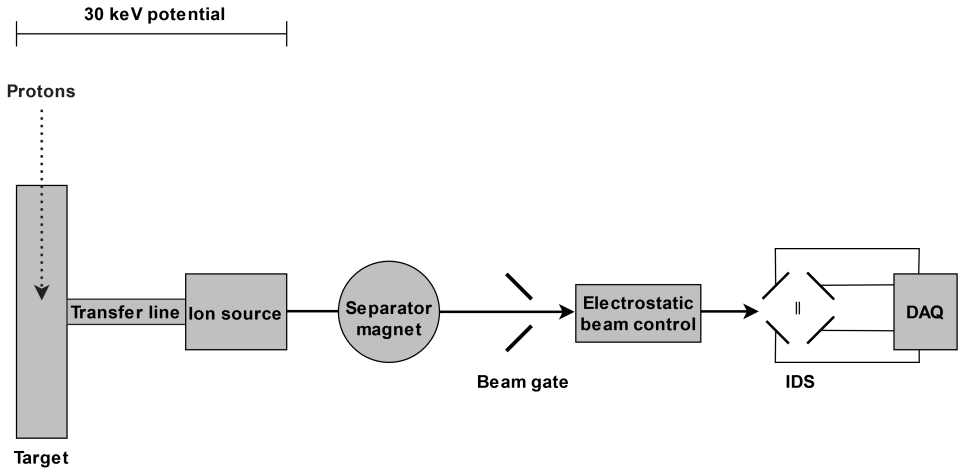

FIGURE 3.2: Production of beam nuclei at ISOLDE and their way to the experimental setup at the IDS. All measurements will be stored by the data acquisition system (DAQ).

BOOSTER typically has energies between 1 to 1.4 GeV [20, 21], and are used to produce the exotic beam isotopes at ISOLDE.

3.1 Production of Beam Isotopes

The beam isotopes used in this experiment, ^{8}He and ^{20}Na, was produced in an uranium carbide target at around 2400 K [22] from a fission process induced by the protons from the PS-BOOSTER. At high temperatures like this the reaction products diffuse out of the target and into an ion source through a cooling transfer line [20, 23]. The cooling transfer line reduces the transfer of less volatile elements, and is therefore good if we want to look at noble gasses such as ^{8}He [24]. From here the ions are accelerated to 30 keV and mass separated before they are distributed to the IDS (ISOLDE Decay Station), where the experiment was executed. This is all depicted on fig. 3.2.

When the desired beam nuclei have been produced and mass separated they will pass through a beam gate. The beam gate can be opened and closed to make sure that as much of the desired beam nuclei are passing through to the experimental setup as possible with as little contamination from other nuclei as possible. The release function (see section 3.1.1) for different nuclei will vary a lot depending on the choice of target and the temperature of the target [25], meaning that different isotopes will arrive at the beam gate at different times. As the mass separator is looking at the q/m (charge over mass) relationship in the nuclei, we can risk to contaminate our sample with other nuclei with the same q/m ratio if the beam gate is left open in the wrong time span. We therefore want the beam gate to be open for as long time as possible without contaminating our sample with other nuclei with the same q/m ratio. For data used in this thesis the beam gate was open in the time span of $T_p = 10$ ms to $T_p = 310$ ms when looking at the decay of ^{8}He. T_p is the amount of time that has passed from the proton as hit the uranium carbide target. We will get back to this parameter later.

3.1.1 The Release Function of ^{8}He

It is important that we understand what happens to the beam nuclei from it is produced in the uranium carbide target till it reaches the experimental setup. During this time the beam nuclei will diffuse out of the uranium carbide target. Futhermore there is a probability that the beam nuclei decay before they reach the experimental setup. These processes can all be described mathematically, which we will attempt to do in the following. As we are primarily interested in the physics of ^{8}He, I will go into detail describing the release function of ^{8}He, but the same concepts can also be applied to other beam nuclei such as ^{20}Na.

From the proton impact in the uranium carbide target to the arrival of the ^{8}He beam in the carbon foil some time will pass. During this time ^{8}He will be produced and diffuse out of the target. We can describe the probability that an isotope of element Z generated at proton impact, $t = 0$, will diffuse out of the target and into the ion source at time t with

$$p_Z(t) = N(1 - e^{-\lambda_r t})(\alpha e^{-\lambda_f t} + (1 - \alpha)e^{-\lambda_s t}) \tag{3.1}$$

where N is a normalization factor, α is the "fast fraction", λ_r, λ_f and λ_s are the rise- fast- and slow-fall time constants, which are all used to describe how fast ^{8}He diffuses out of the target [23].

When ^{8}He has been produced there is a possibility that it will decay before it reaches the experimental setup at the IDS. This decay will have the decay constant λ. The total probability that the an isotope of element Z will reach the experimental setup at time t will therefore become

$$p_{Z,\lambda} = p_Z(t)e^{-\lambda t} \tag{3.2}$$

Eq. 3.2 is called the release function. We can use this release function to describe the amount of ^{8}He reaching the carbon foil at a given time. It is important to understand, that this function can only describe the amount of ^{8}He reaching the carbon foil in the time span where the beam gates are open. After the beam gates are closed, no more ^{8}He will reach the carbon foil.

In the time window where the beam gates are open, ^{8}He will reach the carbon foil at time t with a probability given by the release function. ^{8}He decays in the carbon foil with a probability independent of the release of beam nuclei from the uranium carbide target. We would therefore expect the probability of measuring the decay products of ^{8}He in the DSSDs at time t' to be a convolution between the release function and the decay of ^{8}He:

$$R_{Z,\lambda}(t') = \int_0^{t'} p_{Z,\lambda}(t)N(t, t')\,dt \tag{3.3}$$

Where $N(t, t')$ describes the decay of ^{8}He. We saw examples of such decays in eqs. (2.1) and (2.3).

Chapter 4

The Experiment

In chapter 3 we covered how exotic beam nuclei are produced and transferred to the experimental setup at the IDS. In this chapter we will cover how the experimental setup looks and what happens when the beam has reached the IDS. The data for this experiment was conducted at the IDS for 5 days. In this time span there have primarily been made measurements of the decay of ^{8}He, but there have also been made calibration runs, background runs as well as measurements of the decay of other beam nuclei, such as ^{20}Na. In this thesis I will be looking at around 6.5 hours of data from the decay of ^{8}He, as we in this period of time had all the relevant detectors working at a good resolution.

The data we will be looking at in this thesis will only cover some of the detected elements. As mentioned in chapter 1 this work aims to figure out how much information we can get about the decay of $^{8}\text{He} \rightarrow \alpha + t + n$ when we removed some of the most time-consuming parts of the analysis. The full detector setup contained:

1 INDiE, an array of neutron time-of-flight detectors.

4 Clovers, germanium detectors to detect γ-radiation.

4 DSSDs, double-sided silicon strip detectors to detect charged particles such as α-particles or tritons.

4 Plastics, thick scintillating plastic detectors that can be used to measure electrons from the β-decay of ^{8}He.

Due to the goals of this thesis listed in chapter 1, we will not be looking at any data measured by the Clovers or the INDiE. I did however look at the data from the DSSDs and the Plastics, and in the following section we will be looking further into the experimental setup for these detectors.

4.1 Detector Setup

As I will be looking for αt-coincidences in this thesis, we need to be able to detect charged particles. We can do that with the DSSDs. In this experiment we worked

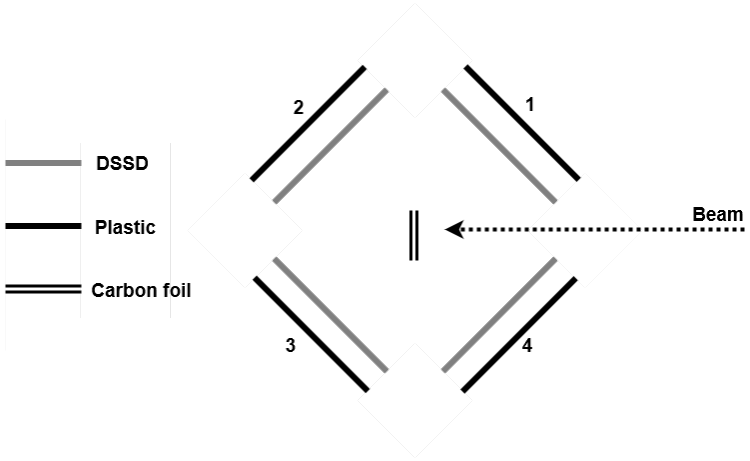

FIGURE 4.1: Illustration of the experimental setup. The numbers indicate the numbering of both the DSSDs and the Plastic detectors.

with 4 50 mm by 50 mm square DSSDs placed as depicted on fig. 4.1. The total solid angle covered by the DSSDs is 30% of 4π. In section 6.4.1 we will discuss the solid angle coverage of the setup further. DSSD 1,3 and 4 had a thickness of 60 μm, and DSSD 2 had a thickness of 65 μm. A DSSD is a segmented detector with 16 vertical strips on one side and 16 horizontal strips on the other side. This gives us a total of 256 pixels in a single detector that can give us spatial information about an energy deposit. A DSSD is a semiconductor detector which means that the energy output from the incoming charged particles in the DSSD comes from the creation of electron-hole pairs. These electron-hole pairs will be able to move freely, and by applying a bias voltage over the detector they will move to the electrodes of the detector, and create an electrical signal which is proportional to the energy of the ionizing radiation [26]. In order to prevent a leakage current to flow through the active layer in the detector a thin front- and back layer is added to the detector. One of these layers will be p-doped and one will be n-doped. These layers will act as dead layers in the detector, as none of the energy deposited in this layer will add to the final electrical signal [27].

Behind each DSSD there is a Plastic detector which is also depicted on fig. 4.1. The plastic detectors is 6 mm thick scintillating detectors. The DSSDs are thick enough to fully stop heavier particles such as α-particles and tritons. Electrons will however only deposit a small amount of energy in the DSSDs. Because of their thickness the Plastics will be able to stop electrons and get an energy and time output from the detector. Whereas the DSSDs has 16 front strips the plastic has 2 front strips. A measurement in the plastic is however only validated if both of the front strips measures a signal. We do therefore not get any spatial information about the detections in the plastics. As we will see in chapter 6 we are only interested in the time-output from the plastics, so the lack of spatial information does not matter.

When the beam reaches the experimental setup at the IDS it has an energy of 30 keV. The beam will reach and be stopped in a carbon foil which has a thickness of 475 nm. The carbon foil is placed in the middle of the detector setup as it can be seen

Isotope	Range [nm]
^{8}He	286.8
^{20}Na	122.1

TABLE 4.1: The range of the different beam types at 30 keV in carbon. These ranges have been calculated with the "Energy Loss Calculator" made by the Aarhus University Subatomic Group [28]

on fig. 4.1. The center of the carbon foil is also set to be the origo of our coordinate system. We will see that the choice of coordinate system will have an effect on how we perceive the angular distribution of the data in section 6.3.

4.2 Deposited Energies in the DSSDs

As we now know how the beam ions are produced and how the experimental setup works, we can now begin to understand what happens when we collect the data. Through the experiment data has been conducted with 2 different beams; ^{8}He and ^{20}Na. The process of conducting data for the two types of beams is the same: The beam will hit the carbon foil, be stopped in the foil and decay. The decay products will then be measured by the DSSDs and plastics. What truly separates the two beam types from each other is the measured energy spectra of the decay products.

As the beam travels through the carbon foil, it will lose energy due to the stopping power of the foil. The sopping power for ^{8}He and ^{20}Na in carbon is different, which means that they will be stopped at different depths in the foil. The ranges of the beam isotopes at 30 keV in carbon can be seen in Table 4.1.

As the beam particles decay inside the carbon foil the decay products will also loose energy on their way out of the foil before they are measured in the DSSDs. As mentioned in section 4.1 the silicon dead layer in the DSSDs also causes the decay products to lose energy before they have reached the active layer of the DSSD. When we measure the energy spectra from the decay products we therefore need to make energy corrections to the spectra to be able to look at the true physical behavior of the beam ion.

This is especially important in the ^{20}Na measurements, as ^{20}Na is stopped only about a quarter of the way through the carbon foil. The spectrum in the upstream detectors will therefore measure higher energies than the downstream detectors. This happens as the decay products travelling towards the downstream detectors will travel further inside the carbon foil and thereby have a greater energy loss. This effect is not as prominent in the data for ^{8}He, as the ^{8}He beam stops about half way through the foil, and the energy loss in all directions is about the same. The physical behavior of the raw ^{8}He data is therefore more reliant even without making any energy corrections. In section 5.1.1 we will see the relevance of making energy corrections on the ^{20}Na data.

4.3 Expected Experimental Results

When doing experimental work, it is always a good idea to consider what we expect to find from our measurements. For example we have in fig. 1.1 seen that 84% of ^{8}He will decay to two α-particles. This is two identical particles, so we would from conservation of momentum expect them to have the same energy and decay in opposite directions (180°) in the CM reference frame. From the figure we can also see that the α-particles will decay through the 3.03 MeV excited state of ^{8}Be, and thereby we would expect the most probable energy measurement of each α-particle would lie around 1.5 MeV.

There is also the probability that we measure two coincident α-particles that does not come from the same decay. This a random occurrence, and we would expect these to have a half-life of half the half-life of the non-random occurrences of $\alpha\alpha$-coincidences, as the rate of measuring two random particles in the time span ΔT is given by

$$R_{\text{Random}} = \Delta T R^2_{\text{Non-random}} \propto e^{\frac{2\Delta T}{t_{\frac{1}{2}}}} \tag{4.1}$$

Where $R_{\text{Non-random}}$ is the rate of the non-random $\alpha\alpha$-coincidences and $t_{\frac{1}{2}}$ is the half-life of ^{8}Li [29].

If we then look at what energies we expect to measure for the αt-coincidences. The total energy release should be given by:

$$Q = E_i - E_f \tag{4.2}$$

Where E_i is the initial energy, which in our case is maximum 9.67 MeV as we saw on fig. 1.1. E_f is the energy of the final level, which is given as 4.5 MeV on fig. 1.1. This means that we would expect the maximum total energy of the α, triton and neutron at around 5 MeV, meaning that we would not expect to measure any individual energies of the alphas or tritons higher than this.

When ^{8}He decays to ^{8}Li we would expect ^{8}Li to experience a recoil from the electron from the decay. When ^{8}Li then decays to two α-particles, we will then meaure this rocoil effect as a slight energy difference between the two α-particles. This effect is most prominent for low-energy α-particles. This means that we would expect the measured energy of the $\alpha\alpha$-coincidences from the decay of ^{8}Li to vary more between the two particles in the lower energy range. This could be a problem as we have also concluded that we expect to measure the αt-coincidences in a lower energy range. We will therefore expect to see a big background induced by the experiment, which we will get back to in chapter 6.

Chapter 5

Preparing the Data for the Analysis

A lot of the work in this thesis has been revolving around data reduction, data analysis and how to sort the measured data in a meaningful way. I will be looking for coincidences between an α-particle and a triton in the DSSDs, and the whole process of doing so will be described in chapter 6. When I received the data-files from ISOLDE they contained information from all detectors about the measured energies, timestamps and detector indexes (a number given to each detector to be able to recognise them from each other). This chapter will go through the preliminary steps of the data reduction process to prepare the data to be analyzed. This means that we will go through what happens to the data from the it was taken, through the calibration and during an energy matching process. To illustrate this better, we can see an illustration of what happens to the data from the conduction of the experiment to the final results has been found in Figure 5.1. This chapter will be covering the two middle stages illustrated on the figure.

5.1 Calibration

As we saw in chapter 3 the data is stored by the data acquisition system (DAQ). The DAQ uses digital data processors called Pixies to translate a detector signal to a channel number. We therefore need to convert each channel number into an energy, which we do with a calibration. During the calibration we measure the energies of well-known radioactive decays. As the DSSDs measure charged particles only, we use α-decays as our source of known radiation.

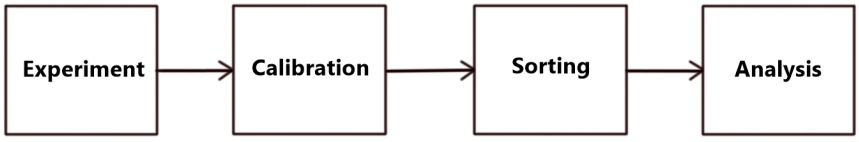

Figure 5.1: An illustration of the data analysis process. Taken from [30].

Isotope	Energy [keV]	Intensity
^{148}Gd	3182.690	1.0
^{239}Pu	5105.5	0.1194
	5144.3	0.1711
	5156.59	0.7077
^{241}Am	5388	0.0166
	5442.80	0.131
	5485.56	0.848
^{244}Cm	5762.64	0.231
	5804.77	0.769

TABLE 5.1: The α-sources used for the calibration, their energies and the intensity of each decay channel. This data comes from [31].

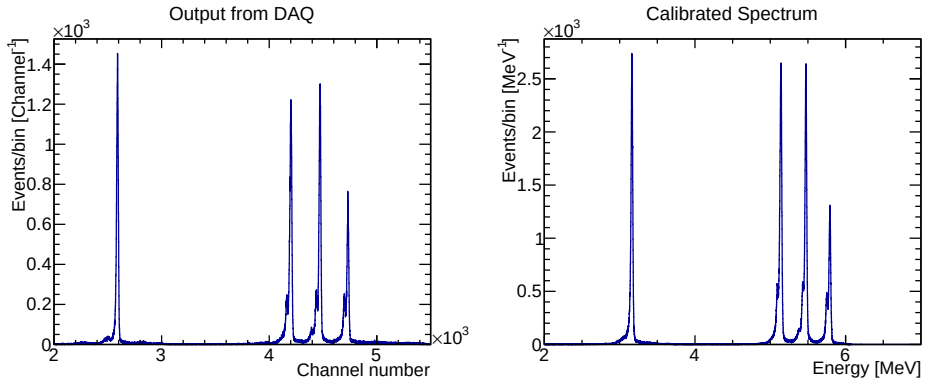

FIGURE 5.2: Spectrum from a calibration run measured by front-strip 12 in DSSD 1. On the figure on the left we see the output from the Pixie. The figure on the right shows the energy- and efficiency calibrated spectrum of the same strip.

The Calibration was done with a 4α-source containing ^{148}Gd, ^{239}Pu, ^{241}Am and ^{244}Cm. The sources were placed on either side of the target holder, and were slid into the middle of the chamber. The α-sources have well known energies known from [31], which make them useful for calibrations. The energies of the α-sources can be seen in table 5.1.

The energy spectrum of the calibration sources was measured for around 90 minutes. From this data a channel-energy calibration as well as an efficiency calibration was done. This was done by finding each peak in table 5.1 whereby they were fitted to a Gaussian as well as corrected to the height of each peak with the information about the peak intensity. A separate calibration was done for all 32 strips in each DSSD. An example of the channel output in a strip from the Pixies as well as a calibrated spectrum can be seen on fig. 5.2.

During the experiment two separate calibration runs were made. The first calibration was done in the beginning of the experiment (run 32), and the other was done in the end of the experiment (run 212). This was done so we could check that the outputs from each calibration run were comparable and did not change over time. I did this

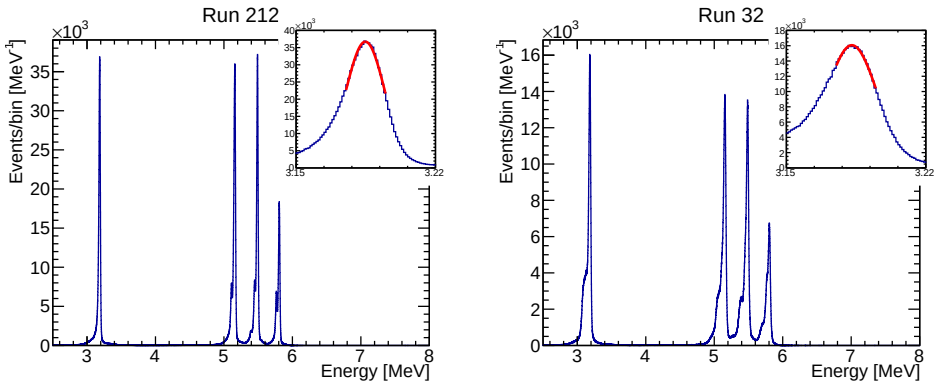

FIGURE 5.3: Energy corrected calibration spectra from the two calibration runs. On the left we see the energy calibrated spectrum of the last calibration run, run 212. In the corner I have zoomed in on the ^{148}Gd peak, where a Gaussian fit has been made to find the mean and the standard derivation of the peak. On the right we see the exact same as on the left, but now we are looking at the energy spectrum of run 32, where the calibration applied comes from run 212 to compare the means of the ^{148}Gd peak.

Run	μ **[MeV]**	σ **[keV]**
32	3.1829	12.921
212	3.1848	9.8524

TABLE 5.2: The the mean, μ, and standard derivation, σ, of the ^{148}Gd peak for both calibration runs.

check by applying the last calibration to data from the first calibration run, and saw how the prominent 3283 keV peak in ^{148}Gd was placed.

To be able to compare the measured energies from two different runs, we had to make an energy correction to the calibrated spectra. As the particles hit the DSSD they travel through their deadlayer described in chapter 4, where they loose some energy due to the Stopping Power. This energy correction is made with the c++ library "AUSAlib" [32] made by the Aarhus Subatomic Group at Aarhus University, which can calculate the energy loss through the dead layer of the detector. On fig. 5.3 we can see the energy corrected calibration spectra of both calibration runs.

From the Gaussian fits to the ^{148}Gd peak in fig. 5.3 we get the mean and standard derivation of the peak for both calibration runs. These values can be found in table 5.2. If we compare the values of the ^{148}Gd peak from table 5.2 to the tabulated value from table 5.1, we can see that the energies found are the same as the tabulated value, when taking the error of the fit into account. It therefore seems to be valid to use the same calibration measurement on all the data files from the experiment.

The ^{148}Gd peak has several advantages as it has an intensity of 1, meaning that we do not see several decay channels overlapping. We have just seen that the peak can be used to check the validity of the calibration on all runs. Furthermore we can also use the peak to determine the standard derivation on the calibration on all data. The ^{148}Gd peak has the advantage that it is not disrupted by any of the other peaks, as

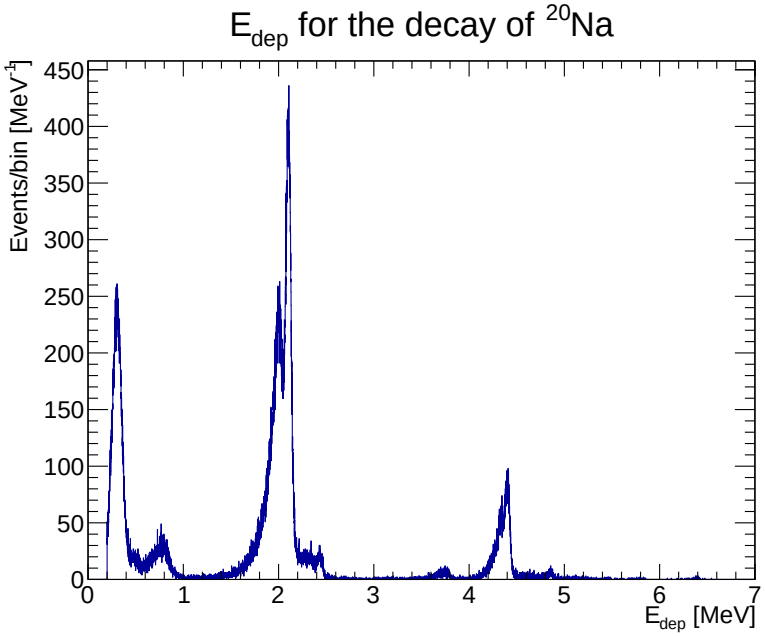

FIGURE 5.4: Deposited energy, E_{dep}, in the detectors from the decay of ^{20}Na.

their energies are much higher. This means that it is easy to fit a nice Gaussian to the peak, and thereby find its width and standard derivation. We can use this to assume that the error is the same on all the measured energies, given by the standard derivation of the ^{148}Gd peak.

5.1.1 Checking the Calibration with a ^{20}Na Measurement

Even though the main part of the experiment was dedicated to measure the decay of ^{8}He, there has been taken around 9.5 hours of data with a ^{20}Na beam. The spectrum of ^{20}Na is measured with high statistics in [33], and is therefore a good source to use, when we need to investigate some unknown variables in the ^{8}He data. I will therefore throughout this thesis be using the ^{20}Na measurements as a sanity check on some of my conclusions. As my first sanity check, I will check my calibrations on a ^{20}Na run.

As we saw in Table 4.1, ^{20}Na has a shorter range in the carbon foil than ^{8}He. This means that the energies measured in the upstream- and downstream detectors will be different. This energy difference is depicted on fig. 5.4, where we can see that the measured energy peaks are wide. Around 2 MeV we can also see two peaks close to each other. These comes from the same unbound state in ^{20}Ne, but as the energy loss is bigger for particles detected in the downstream detectors, the energy peak will be slightly shifted. When looking at the measured energies from the ^{20}Na spectrum, it is therefore important that we apply energy corrections from the energy loss in the target and in the deadlayer of the detector as explained in section 4.2.

On fig. 5.5 we see the excitation spectrum of ^{20}Ne. We are interested in looking at the excitation spectrum of ^{20}Ne, as it is the excitation energies from the decay of ^{20}Na

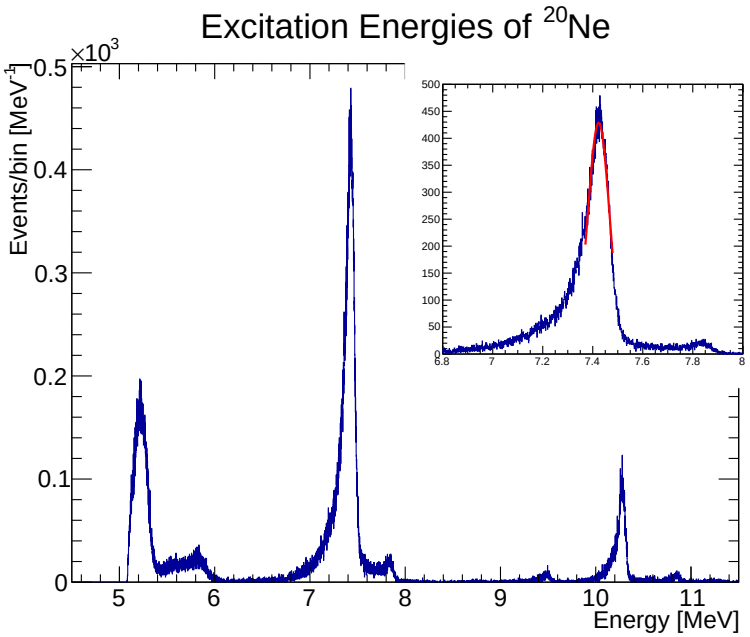

FIGURE 5.5: Measured excitation spectrum of ^{20}Ne from the β-decay of ^{20}Na with a fit to the most prominent peak around 7.5 MeV

that has been found in [33]. We measure the kinetic energy of the charged particles with the DSSD, and we therefore have to make a conversion of the of the energy corrected spectrum with eq. (2.15). The α-separation energy of ^{20}Ne is $E_{\text{sep},\alpha} = 4.730$ MeV [33].

From the fit in fig. 5.5 we get that the main peak in the ^{20}Ne excitation spectrum has an energy of (7.42 ± 0.0434) MeV compared to the value of (7.422 ± 0.100) MeV in [33]. These values are very comparable, and we can therefore conclude that we from this second check of the calibration have a very good calibration that we can trust for the rest of the experiment.

5.2 Sorting of Data

When the calibration is done the next step in the data reduction process is sorting the data. The sorting process is done by the Sorter from the AUSAlib library [32]. The purpose of the sorting process is twofold:

1. The calibration is applied to the to data files.
2. DSSDs will go through front/back-matching.

In this step we look at the front- and back strips of the DSSDs and match the energies they have measured. In this process energies measured in the front strips are compared to energies measured in the back strips. The pairs with the lowest energy difference is the most probable and is therefore matched to be a single hit. This process is called front/back-matching and is illustrated on fig. 5.6.

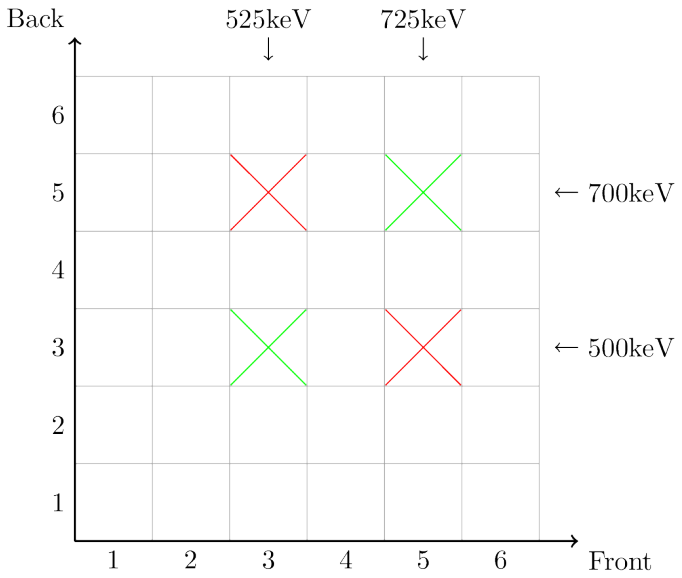

FIGURE 5.6: The concept of front/back-matching illustrated by a 6x6 grid. The grid represents the intersection of six front and back strips in a DSSD. In the front strip energies of 525 keV and 725 keV has been detected. In the back strip energies of 500 keV and 700 keV has been detected. All the different energy combinations is shown. In the sorting process the pairs with the lowest energy difference is matched. A match is marked with a green cross. The figure comes from [34].

When a front/back pair has been made the sorter gives it an exact coordinate position by assuming that all hits in a pixel is uniformly distributed over the pixel surface. It is also in this step we can disable dead or low-resolution strips in the detectors if needed. After the data has been through the sorter we can now begin our analysis of the data.

Chapter 6

Data Analysis

When the data has been front/back-matched and sorted, we have a set of data that we trust to be a true reflection of the physical reactions happening in the experiment. In this chapter, I will be covering the last stage in fig. 5.1: The process of analyzing the sorted data. As we will see, this process is no easy matter, as we come across different challenges when looking for particle coincidences in different directions. As mentioned in chapter 1, we are interested in finding αt-coincidences from the reaction shown in eq. (1.2). The aim of this chapter is therefore to find coincidences between particles and determine whether they are an αt-coincidence or something else.

We would expect to see different behaviour of coincidences depending on the angle between the incident particles. As we saw in section 4.3, ^{8}Li decays to two α-particles in a 180° angle in the CM system. We would therefore only expect to see ^{8}Li in coincidences with angles close to 180° in the lab. We will be measuring the α-particles from this decay, which will give us a source of background for coincidences which is separated with around 180°. If we on the other hand are looking for coincidences in other directions, we would not expect to see this effect. I will therefore categorize all the coincidences into 3 categories:

0° coincidences:
These coincidences are found in the same detector. Coincidences of this type are illustrated in fig. 6.1a.

90° coincidences:
These coincidences are found in detectors placed 90° from each other. Coincidences of this type are illustrated in fig. 6.1b.

180° coincidences:
These coincidences are found in detectors placed 180° from each other. Coincidences of this type are illustrated in fig. 6.1c.

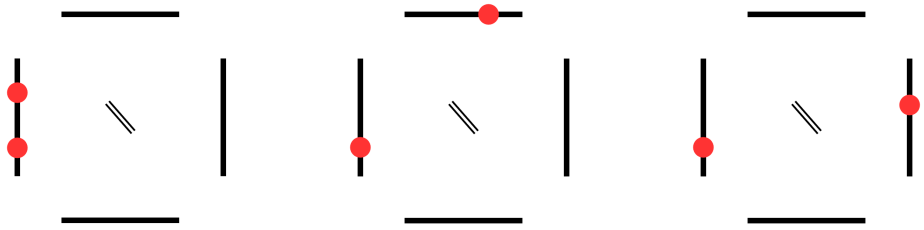

(A) 0° coincidence. (B) 90° coincidence. (C) 180° coincidence.

FIGURE 6.1: Overview of the different types of coincidences. (A) shows a 0° coincidence, which is two particles detected in the same detector. (B) shows a 90° coincidence, which is two particles detected in detectors placed 90° from each other. (C) shows a 180° coincidence, which is two particles detected in detectors placed 180° from each other

As we will see, the energy distributions of coincidences in these 3 coincidence categories are all different, and therefore the treatment of the coincidences will be different. We will in sections 6.1 to 6.3 go through the different treatments of the data, but first we will be looking at the analysis process in itself, and the common steps for all the coincidence types.

Before we can make further analysis on the different particle coincidences, we first need to understand what defines a coincidence in this work. Some of the detectors act as triggers for the experiment, which means that a timer will be started when the detector is triggered. A time window of around 3500 ms will then be open, and everything detected in this time-span will be regarded as an event. This also means that we can only allow a coincidence between two particles to be valid, if it happens during the same event. For now this will be our only criterion for a particle coincidence, but more will be added later. This also means that we can throw events away where only a single particle has been measured in the DSSDs.

Another concern we have to deal with is the possibility of measuring an electron in the DSSDs. This electron would come from the β-decay of ^{8}He. To make sure that we do not confuse an electron for an α or a triton, I will therefore check whether a particle detected by a DSSD is in coincidence with with a particle detection in the plastic behind the DSSD. For this process I have chosen to only look at particles with a DSSD multiplicity of 2. This means that I have removed data sets where more than 2 particles have been detected in the DSSDs even though two of these particles very well could be an α-particle and a triton. This choice has been made, as it is complicated to find out which two particles belong to the same decay. Furthermore we can on fig. 6.2 see that most of the data with multiple detections in the DSSD has a DSSD multiplicity of 2.

From this β-coincidence analysis we have 3 possible outcomes:

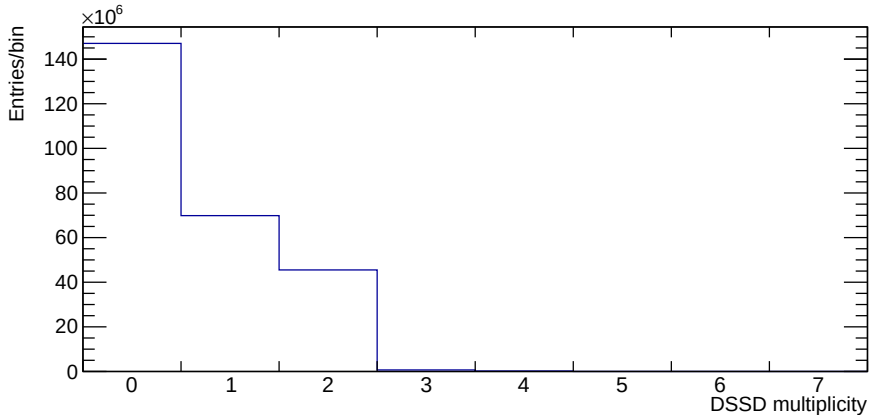

FIGURE 6.2: Histogram of the DSSD multiplicity from each entry in the detector.

1. Both detected particles in the DSSD are in coincidence with a detection in the plastic behind the DSSD. This means that there is a chance that both particles detected by the DSSD are electrons.

2. One of the two detected particles in the DSSD is in coincidence with a detection in the plastic behind the DSSD. This means that there is a chance that one of the particles detected by the DSSD is an electron.

3. None of the detected particles in the DSSD are in coincidence with a detection in the plastic behind the DSSD. This means that we can be certain that we have not detected an electron in the DSSD.

It is important to note that this analysis is not determining whether we measure electrons or not, as the coincidences with a plastic detector could also be a random occurrence. The process of this analysis is illustrated in fig. 6.3. As we do not know the decay of ^{8}He well, I did this analysis on both ^{8}He data as well as ^{20}Na data. As mentioned in section 5.1.1 we can use the measurements of ^{20}Na to investigate unknown variables, as the ^{20}Na spectrum is well-known with high statistics. If we look at fig. 6.4, we can see the result of the β-coincidence analysis for ^{20}Na.

As it can be seen on fig. 6.4, the energy distribution of the particle pairs which are also in coincidence with an electron detected by the plastic, is seemingly the same as the energy distribution of the particle pairs which are not in coincidence with any electrons. This must mean that we have not detected any electrons in the DSSDs and we can therefore expect to only measure α-particles and tritons in the DSSDs.

We do not know much about the spatial distribution of the neutrons, α-particles and tritons from the decay of ^{8}He. As an α-particle and a triton is similar in size, we would expect them to decay close to back-to-back. This has in fact been observed in a yet unpublished experiment [35]. The question is now: Can we find similar results for the 180° coincidences in this experiment? And will we be able to find αt-coincidences in other angles? If we expect the same results as in [35], we will

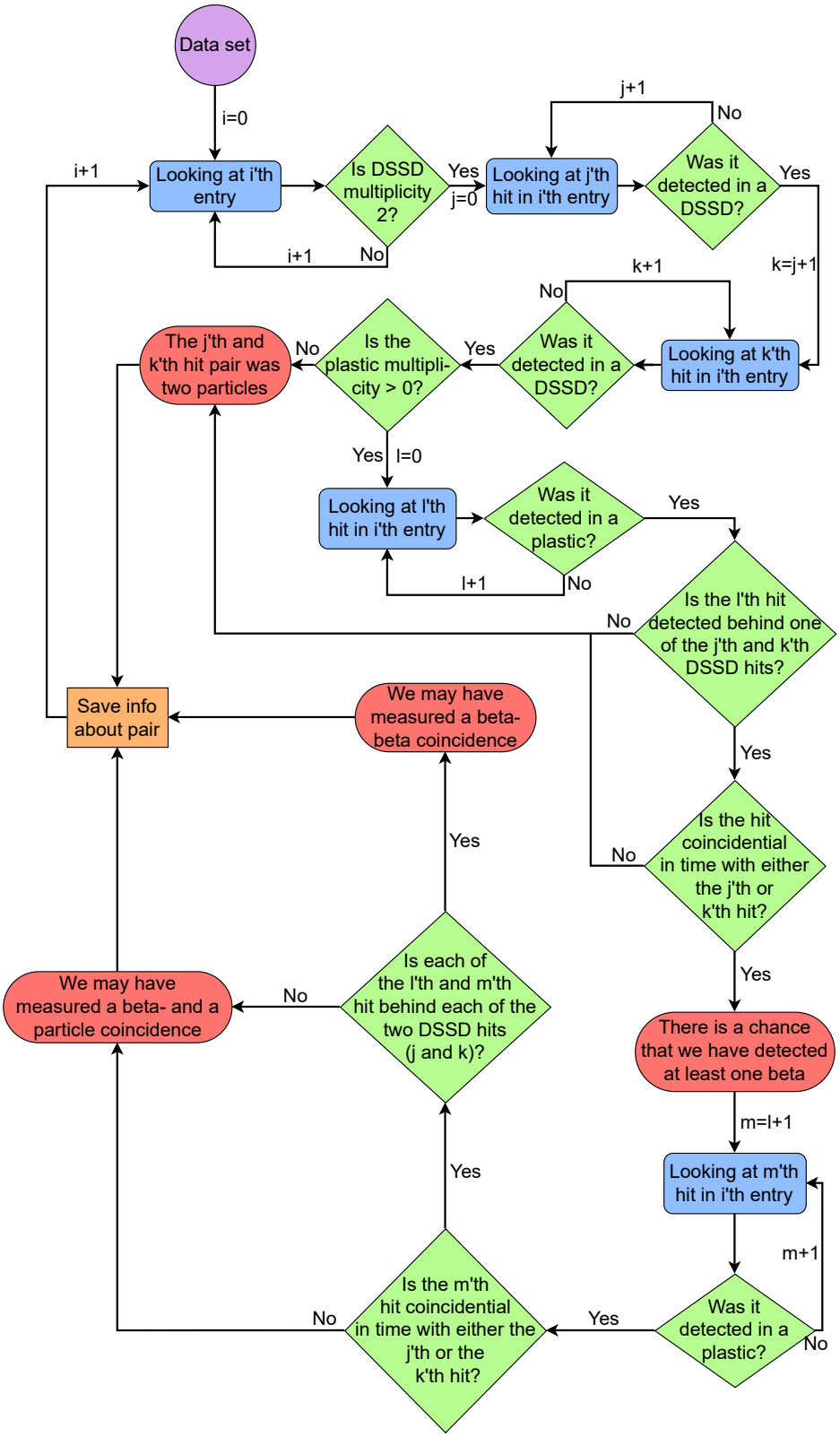

FIGURE 6.3: Overview of β-coincidence analysis for entries with 2 detected DSSD hits. The purple circle represents a whole data set that I want to investigate. All the blue rounded boxes give an overview of where we are in the analysis process and all the green diamond shapes are an action that helps us sort through the data. If we make it to one of the red oval shapes, we have acquired some knowledge of a hit pair, which will be saved in an output file, potentially after even further analysis. Every time a letter is increased by 1 it indicates that we are looking at a new combination of data.

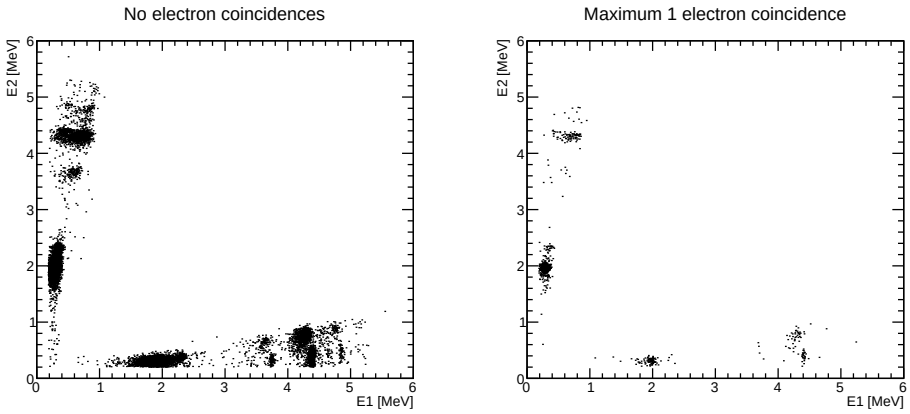

FIGURE 6.4: Energy distributions for coincidences in ^{20}Na data. $E1$ and $E2$ are the detected energy of each of the two particles in the coincidence. On the left we see the energy distribution for the particle pairs that did not have any coincidences with a detection in a plastic. On the right we see the energy distribution for the particle pairs that did have a single coincidence with a detection in a plastic. The energy distribution for particle pairs which are both coincident with a plastic detection is not shown, as none was found.

not find any αt-coincidences in 0° and 90° regime. With this knowledge we can now move on to look for αt-coincidences from the decay of ^{8}He. In the following sections I will go through the processes I have been through in order to assess the data and gather information from it. Some methods and techniques will be used more than once, but will only be described in detail the first time I use it.

6.1 0° Coincidence Analysis

We will start by looking at coincidences in the same detector. For coincidences in the same detector, we expect to only measure random coincidences from the $\alpha\alpha$-decay from ^{8}Li as well as the possible αt-coincidences. The random coincidences does not belong to the same decay, and we would therefore expect them to be evenly distributed over time. We would expect real coincidences to be detected around the same time, meaning that the difference in time of detection should be very small. If a pair lives up to this, I will from now on refer to them as correlated in time. On fig. 6.5 we can see this behavior illustrated on the data from coincidences in the same detector.

As we can see on fig. 6.5 there are several peaks, not just around 0 ns. As we expect the random background to be uniformly distributed, these peaks must all be valid coincidences. That all valid coincidences does not lie around 0 ns can be explained by the cabling of the detectors. Each strip in each DSSD is connected to a computer, and the time we see plotted in fig. 6.5 is dependent on this cabling. In theory we should make a time calibration for all strips to make sure, that the time measurement in all DSSD strips has the same point of origin. This process is however time consuming, and has therefore not been prioritised in this work as mentioned in chapter 1. Instead, I will only be looking at the data at the main peak around 0 ns, meaning that a valid coincidence must have $\Delta T < 1500$ ns.

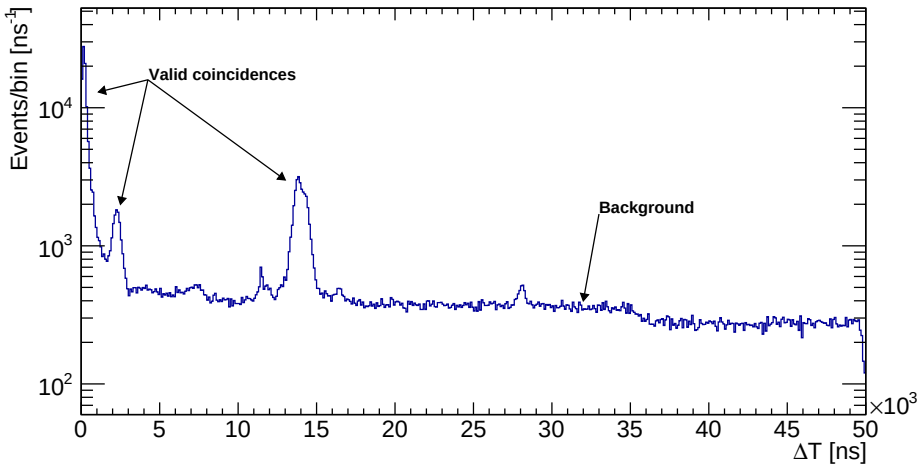

FIGURE 6.5: A histogram of the absolute time difference in ns, ΔT, between 2 events in the same detector. No cuts have been made in this data.

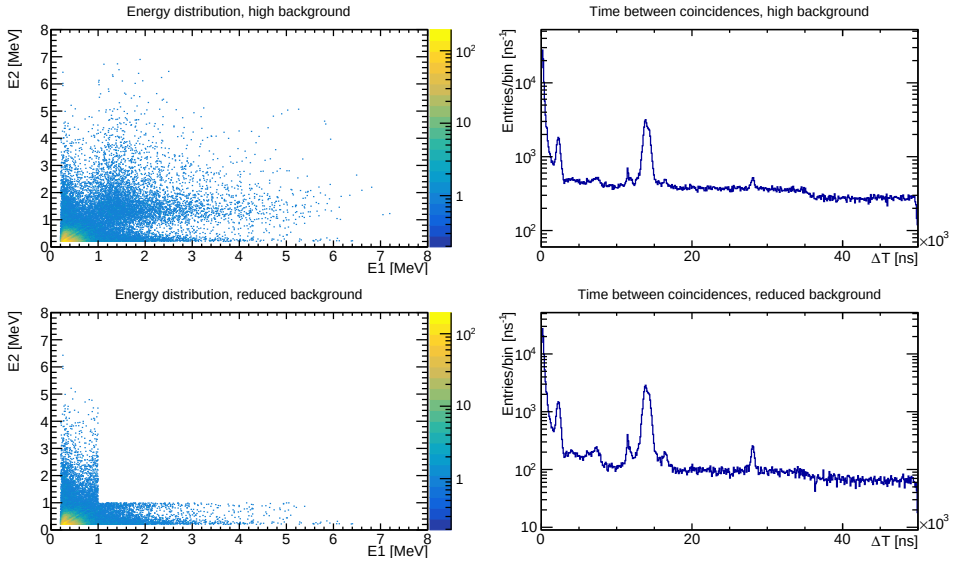

FIGURE 6.6: Upper left: Energy distribution of 0° coincidences with $\Delta T < 1500$ ns. Upper right: Time between measurements of coincidences in the same detector. The two lower figures is the same as the above, but now energies of > 1 MeV for both coincidences has been discarded. We can see that the background in the data has become much lower by removing these energies, while the peaks has the same or a better solution.

As we have discussed in section 4.3, the energy spectrum of a single α from the $\alpha\alpha$-decay from ^{8}Li peaks around 1.5 MeV. We would therefore expect most of the random coincidences to have at least one of the particles have an energy of around 1.5 MeV. As we can see on fig. 6.6, the amount of random coincidences is much smaller if we remove all energies of > 1 MeV while the peaks remain about the same height.

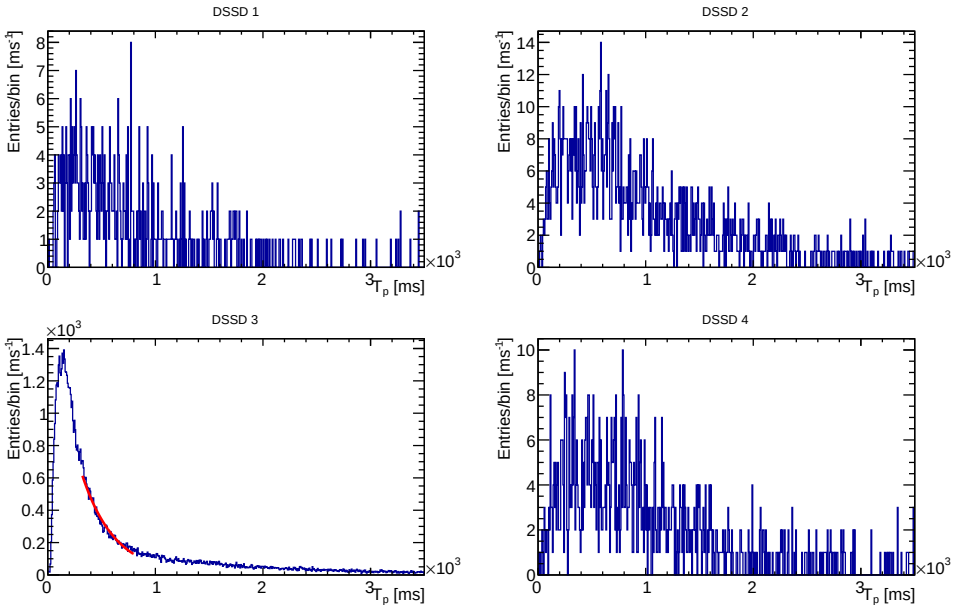

FIGURE 6.7: T_p spectrum for 0° coincidences in the four DSSDs.

On the bottom of fig. 6.6 we have removed as much of the background as we can without loosing any information about the valid decays. There is therefore a possibility that this data contains αt-coincidences. In order to check this, we can look at how much time has passed since the protons from the PS-BOOSTER has arrived to the uranium carbide target. We will call this time T_p. As we saw in section 3.1.1, we can describe the probability of measuring the decay of ^{8}He at time $T_p = t$ as a convolution of the release function and the decay of ^{8}He. When the beam gates are closed we will only see the decay of ^{8}He. So if the amount of decays after the beam gates have closed can be described with the the exponential decay law in eq. (2.1) for ^{8}He, we must have had αt-coincidences.

On fig. 6.7 we see the T_p spectrum for the 0° coincidences in each DSSD. What is worth noticing is that the spectrum in DSSD 1, 2 and 4 have less data than the spectrum for DSSD 3. Furthermore it seems that the data for DSSD 3 peaks earlier than for the rest of the detectors. It could even seem that the spectra we measure is from completely different decays. On fig. 6.7 we can see a fit for the data from DSSD 3 to the exponential decay law shown in eq. (2.1). From the fit we get that $t_{\frac{1}{2}} = (212 \pm 3.68)$ ms, which does not match with the tabulated value of 119.1 ms for the half-life of ^{8}He [31]. It does however, fit even worse with the tabulated value of the half-life of ^{8}Li of 839.9 ms [31], so it does not seem that we have measured 2 low-energy α-particles. This data could potentially be αt-coincidences in a background of random $\alpha\alpha$-coincidences. This is what we assume for now. In chapter 8 this will be discussed further, as it is also a problem that this behavior is only observed in a single DSSD.

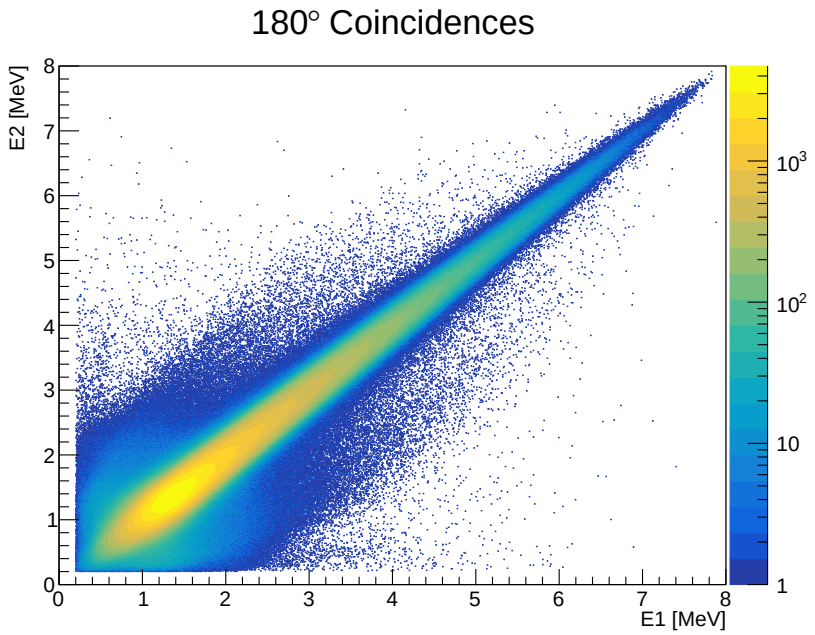

FIGURE 6.8: Energy distribution of 180° coincidences with $\Delta T < 1500$ ns.

6.2 180° Coincidence Analysis

From [35] we know that we can expect to find αt-coincidences in the 180° coincidence data. We do however, have a small problem, as we now have an extra source of background to our measurements. This background comes from the $\alpha\alpha$-decay from ^{8}Li. In section 6.1 we saw that this decay only provided us with a background of random coincidences, but we will now see a background of both random and time correlated coincidences of the $\alpha\alpha$-decay. This happens as the alphas will decay with an angle of 180° between them in the CM system, as explained in section 4.3. On fig. 6.8 we can see the energy distribution of the time correlated coincidences with a $\Delta T < 1500$ ns. The thick diagonal is the non-random $\alpha\alpha$-coincidences from the decay ^{8}Li.

Right now we are able to reduce the amount of random coincidences as we saw in section 6.1, but we need to find a way to deal with the time correlated coincidences from the $\alpha\alpha$-decay from ^{8}Li. The best way to remove this background would be to find coincidences between the α-particle, the triton and the neutron. As mentioned in chapter 1 it has not been prioritised in this work. It would, however, have been the ideal way to remove most of the background in this data set. The task is now to figure out if there are any other possible ways to remove as many of the $\alpha\alpha$-coincidences without loosing too much information about the αt-decays. We could try to remove all the data on the diagonal, but as mentioned in section 4.3 the biggest β-recoil is for low-energy $\alpha\alpha$-coincidences. We will therefore have to remove a lot of data points, without being totally sure that we have removed the background from the $\alpha\alpha$-decay.

What I have done instead is to look at the angular distribution of the coincidences before and after we have sorted them with the $\Delta T < 1500$ ns requirement. On fig. 6.9

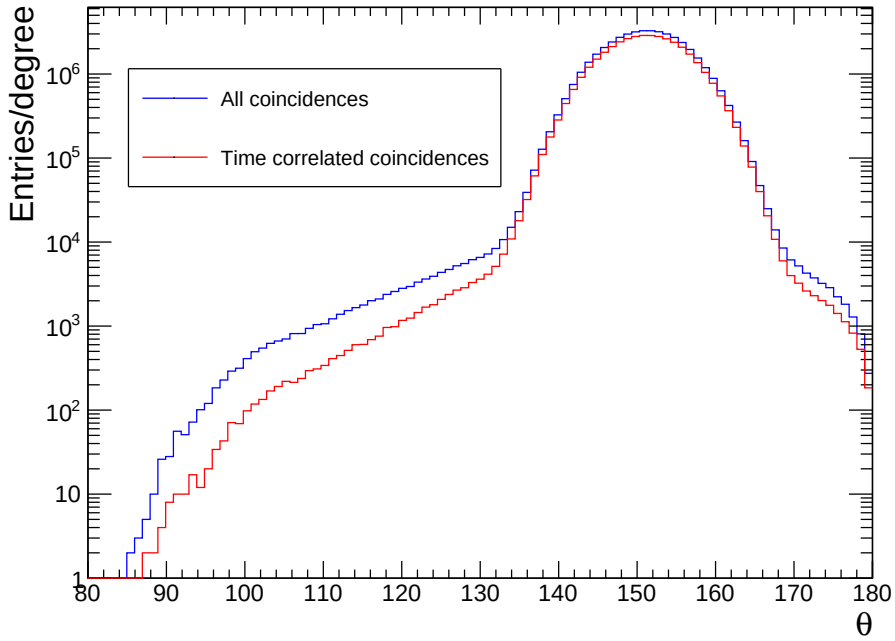

FIGURE 6.9: Angular distribution of the 180° coincidences, where θ is the relative angle between the 2 particles in a coincidence. The blue line is all the possible coincidences, and the red line is the time correlated coincidences with $\Delta T < 1500$ ns.

we can see that a lot of data is still left in the angles $< 130°$, which must indicate that we have some non-random coincidences in there.

If we look at these coincidences and remove all energies > 2 MeV in both detectors to get rid of the last coincidences on the diagonal we get the energy and time (T_p) distributions shown in fig. 6.10 As we can see this gives us a quite uniform energy distribution i the lower energy region. Once again we will look at the T_p distribution of this data which we can see in fig. 6.11. I have made a fit to the time distributed data after the beam gates was closed at $T_p = 310$ ms as we have seen in section 6.1 as well. Here we get $t_{\frac{1}{2}} = (173 \pm 3.62)$ ms compared to the tabulated value of 119.1 [31]. These values are not the same, but as we can see on fig. 6.10 there is a background in the data of random coincidences, which can bring up the measured half-life, as the spectrum is not free of noice. There is therefore a good reason to believe, that this data primarily contains αt-coincidences with a small background from $\alpha\alpha$-coincidences.

6.3 90° Coincidence Analysis

For the 90° coincidences we would only expect a background from the random $\alpha\alpha$-coincidences as we saw for the 0° coincidences. This is however not what happens. If we look at the energy distribution of the time correlated coincidences, coincidences with $\Delta T < 2500$ ns on fig. 6.12, we see that we still have coincidences on the diagonal,

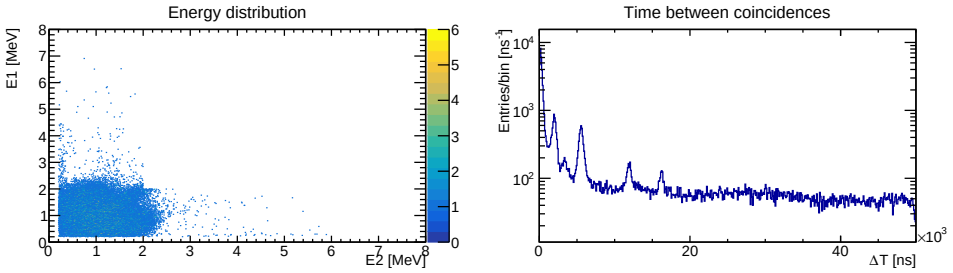

FIGURE 6.10: Left: Energy distribution of 180° coincidence data after as much background as possible has been removed. Right: ΔT spectrum of the same data.

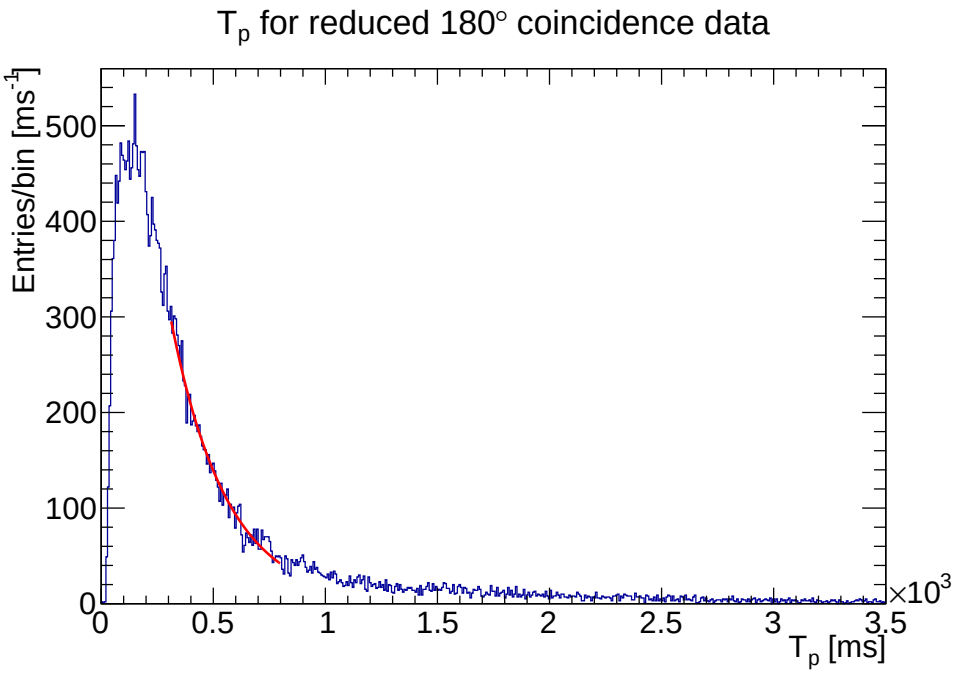

FIGURE 6.11: T_p spectrum of 180° coincidence data after an attempt to remove as much of the known background as possible.

as we saw in the 180° coincidence data. We need to understand what this data on the diagonal is. In the next section I will describe my process of investigating this data in order to reach the conclusion that what we observe is ^{8}He diffusing out of the carbon foil.

6.3.1 ^{8}He Diffusion

We will now be looking further at the data on the upper diagonal on fig. 6.12, as we would not have expected to see such a prominent tendency in this area in the data for 90° coincidences. As explained in section 4.3, the decay of ^{8}He will send two α-particles in the opposite direction of each other, and should therefore not be found at a 90° angle, but if we look at their angular distribution, they will in fact have an angle at around 80° to 130° between each other as we can see on fig. 6.13a. In comparison we saw that most of the $\alpha\alpha$-decays in section 6.2 had a relative angle

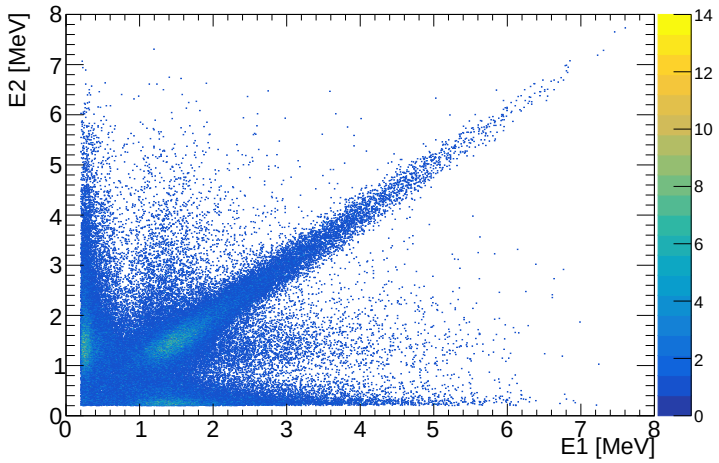

FIGURE 6.12: Energy distribution of 90° coincidences with $\Delta T < 2500$ ms.

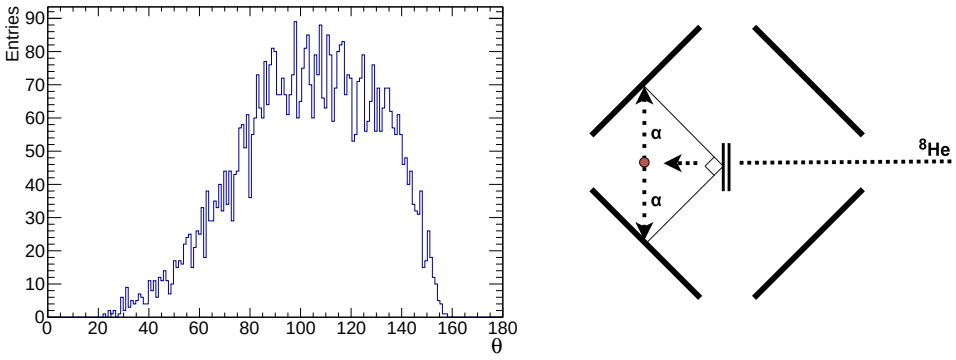

(A) Anglular distribution of the upper diagonal data ($E_1 > 2.5$ MeV and $E_2 > 2.5$ MeV) from the 90° coincidence data.

(B) Illustration of the concept ^{8}He diffusion.

FIGURE 6.13: Potential explanation for the upper diagonal data on fig. 6.12. On (A) we see the angular distribution of the data on the diagonal where θ is the relative angle between the 2 particles in a coincidence, and on (B) an illustration of ^{8}He diffusion. In the diffusion process ^{8}He will leave the target and decay outside the carbon foil. Depending on how far ^{8}He travels from the carbon foil, we will measure different angles between coincidences. On this figure it is illustrated how it is possible to measure a 90° angle between the 2 detections even though the 2 alphas decay back-to-back in a 180° angle in the CM system.

of around 145° to 165° between them. These angular distributions must therefore come from different effects.

A possible explanation for this behavior will be that ^{8}He diffuses out of the carbon foil. This would make it possible for the angle between the two coincidences to be severely under 180° as illustrated in fig. 6.13b. As our coordinate system has its origo in the center of the target where ^{8}He should be stopped and decay, the angle between the alphas is not calculated from where they actually decay, but from where we expected them to decay. If ^{8}He has in fact diffused out of the carbon foil, we

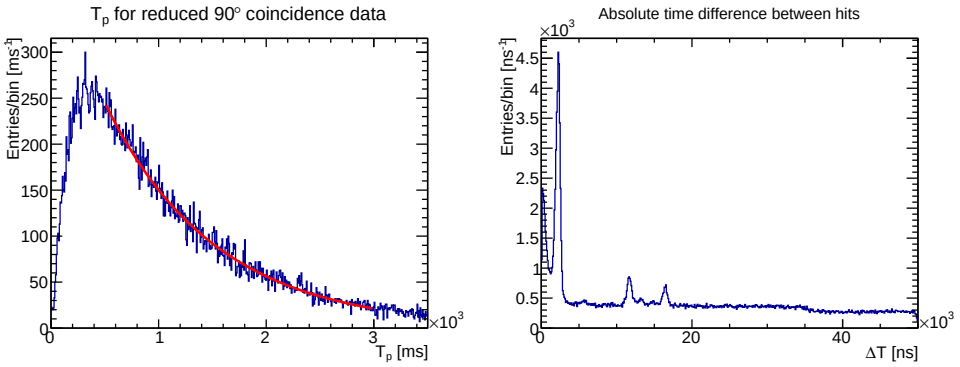

FIGURE 6.14: Left: T_p spectrum of 90° coincidence data after an attempt to remove as much of the known backgrounds as possible. On the figure we see a fit to the downward slope in an attempt to find the half-life of the data. Here we get $t_{\frac{1}{2}} = (707 \pm 6.37)$ ms. Right: ΔT spectrum of 90° coincidence data after an attempt to remove as much of the $\alpha\alpha$-coincidences from the decay of ^{8}Li.

would expect the mean lifetime of the data on the upper diagonal to be larger than the mean lifetime of all the data. We do not have the means to directly check the mean lifetime, but we can check how long time has passed since the protons from the PS-BOOSTER arrived at the uranium carbide target. Here we get that the data on the upper diagonal has a mean $T_p = 1203$ ms and all the data has a mean $T_p = 1056$ ms. As expected we see that the upper diagonal has bigger mean, meaning that the mean lifetime of the ^{8}He on the diagonal was longer as well. We can thereby conclude that ^{8}He has diffused out the carbon foil, meaning that the data on the diagonal is from the decay of ^{8}Li, and is therefore a background we need to remove from the 0°-coincidence data. If we compare how many $\alpha\alpha$-coincidences we see in 90° compared to 180° they only account for 0.13% of all the time correlated $\alpha\alpha$-decays, so this is an overall small effect.

6.3.2 Further Analysis of 0° Data

Now that we know that the upper diagonal we see on fig. 6.12 is ^{8}He diffused out of the carbon foil, we now know that we have two types of background from the data:

Random $\alpha\alpha$-coincidences from the decay of ^{8}Li.
: This was removed as much as possible by only including the time correlated coincidences, which was coincidences with $\Delta T < 2500$ ns.

^{8}He which has diffused out of the target.
: This has not yet been removed, but the most effective way of removing it will be to remove all data that satisfies $|E_1 - E_2| < 500$ keV, which is all the data on the diagonal.

When all the data on the diagonal is removed we can begin to look at some of the other information we have about the coincidences. On fig. 6.14 we can see a plot of T_p as well as a plot ΔT, for our data when the random $\alpha\alpha$-background as well as the $\alpha\alpha$-coincidences from the diffusion of ^{8}He is removed. The T_p distribution

can tell us something about composition of the data. As we have earlier discussed, the T_p spectrum is dependent on the release function in the time where the beam gate has been open, and when the beam gate has closed the T_p spectrum will be dependent on the decay of the mother nucleus of the measured particles. For the data on fig. 6.14 the half-life is found by eq. (2.1), and is found to be $t_{\frac{1}{2}} = (707 \pm 6.37)$ ms. This half-life value does not match the half-life of either ^{8}He (119.1 ms) or ^{8}Li (839.9 ms) [31]. As the value of the half-life is much bigger than for the half-life of ^{8}He, and I therefore do not seem to have found any αt-coincidences in 90°. I will discuss this further in chapter 8.

6.4 Finding Branching Ratios

Now that we have found some possible αt-coincidences, we would like to determine the branching ratios of these observations. We can find the branching ratio by

$$BR = \frac{N_{\alpha t,\text{tot}}}{N_{^8\text{He}}} \tag{6.1}$$

where $N_{\alpha t,\text{tot}}$ is the total estimate of how many αt-coincidences was found after a solid angle correction has been done and $N_{^8\text{He}}$ is the total estimate of how many ^{8}He decays that took place after a solid angle correction.

Right now we have some observations of αt-coincidences from sections 6.1 and 6.2. These observations will have to undergo a solid angle correction before we can use them in eq. (6.1). Before we talk more about these solid angle corrections, I would like to talk about how we will find the total number of ^{8}He that reached the carbon foil. Again, without doing any solid angle corrections for now.

To find the total number of ^{8}He that reached the carbon foil, we will utilize the prior knowledge we have of the decay of ^{8}He. From the literature it is known that 84% of ^{8}He will decay to the first excited state of ^{8}Li [8] as depicted on fig. 1.1. 100% of the particles ending up in the first excited state of ^{8}Li will decay to through the $\alpha\alpha$-branch with ^{8}Be as a compound nucleus [31]. This means that we will be able to determine how much ^{8}He that reached the carbon foil by

$$N_{^8\text{He}} = \frac{100}{84} N_{^8\text{Li,tot}} \tag{6.2}$$

where $N_{^8\text{Li,tot}}$ is the number of ^{8}Li after correcting for solid angle efficiencies.

We therefore need to find all the $\alpha\alpha$-decays from ^{8}Li to get an accurate estimate of how much ^{8}He reached the carbon foil. We will do this by accepting time correlated coincidences with relative angles of $\geq 130°$ and energies that satisfy $|E_1 - E_2| < 500$ keV as $\alpha\alpha$-decays from ^{8}Li. In other words, this will be the data on the diagonal in fig. 6.8. To confirm that we are in fact looking at the $\alpha\alpha$-coincidences from the decay of ^{8}Li, we will look at the T_p spectrum of this data, which can be seen in fig. 6.15. A fit to the data was made, and the half-life of the data was found to be 916.6 ± 1.002 ms. This value is slightly higher than the tabulated half-life of ^{8}Li at 839.9 ms [31]. The difference between these half-lives is however small enough that we can expect to have found $\alpha\alpha$-coincidences from the decay of ^{8}Li.

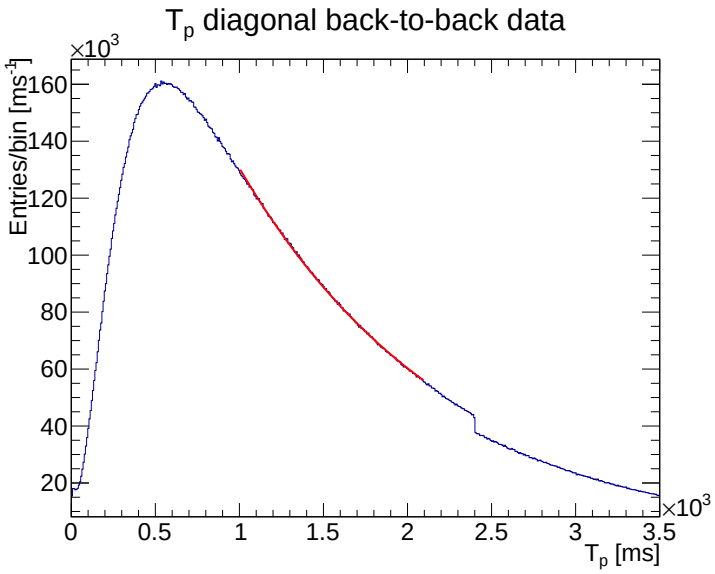

FIGURE 6.15: T_p distribution of the data that is supposed to be $\alpha\alpha$-coincidences from the decay of ^{8}Li. The jump in the data just before 2500 ms is caused by the data acquisition system, as the window for measuring data has been closed too early some of the time. The red line is a fit to the data which gave us a half-life of 916.6 ± 1.002 ms.

6.4.1 Solid Angle Corrections

When doing an experiment we would ideally be able to take measurements in every direction. In reality we use detector setups that can only measure a particle, if it hits the detector's active layer, meaning that we can only cover a certain percentage of space. What we usually do to represent "all space" is to enclose the center of our coordinate system by a circle of radius 1. The surface area will then be 4π and will represent the maximum amount of space that we will be able to cover. We can then look at each pixel in each DSSD, and calculate the solid angle subtended by each pixel by seeing each pixel as a rectangle of dimensions $l \cdot b$, a distance d away from the center of the coordinate system. This calculation has been done with [36] and tells how much of space we cover with every single pixel in each DSSD.

If we were only looking for a single particle we could use these calculations to do an efficiency correction on all the data. We do however need to make an efficiency correction for coincidences between 2 particles.

We give all pixels in the detector setup a different number. We then measure two particles, p_1 and p_2, in pixel i and j respectively. Each pixel covers an amount of the whole room with each of their solid angles. We can then calculate the total efficiency for the particles to hit the i'th and the j'th pixel in the detector setup by

$$\epsilon_{p_1 p_2} = \begin{cases} 0 & i = j \\ \Omega_i \Omega_j & i \neq j \end{cases} \tag{6.3}$$

where Ω_i and Ω_j is the solid angle of the i'th and j'th pixel in the setup [37]. Notice that we cannot measure two particles in the same pixel. When we find the angle

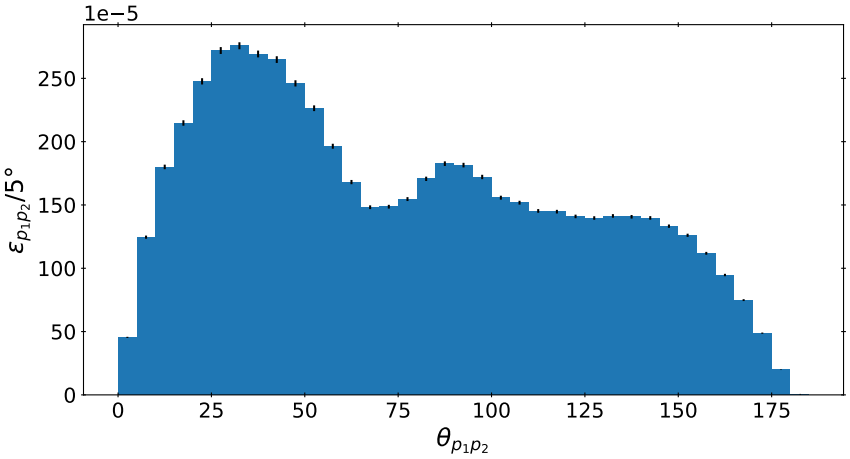

FIGURE 6.16: Efficiencies of 2-particle detections per 5° calculated with eq. (6.3). The angle, $\theta_{p_1p_2}$, is the relative angle between the two particles. The uncertainty is found to be $< 1\%$ when the uncertainty in the placement of the detectors is set to be 0.5 mm. To take account for uncertainties on placement of the beamspot the total uncertainty of the efficiencies is set to be 1%.

between all the possible combinations of pixels this gives us the spatial efficiency depicted on fig. 6.16.

We can now take the data we want an efficiency correction on and look at the angular distribution of the data itself. We will then correct each bin in the data with the corresponding efficiency coefficient from fig. 6.16. In other words the efficiency corrected number of detections will be given by

$$N_{\text{corrected}} = \sum_k \left(\frac{N_{\text{measured}}}{\epsilon_{p_1p_2}} \right)_k \tag{6.4}$$

where N_{measured} is the number of detections in the k'th bin of the angular distribution of the data.

We can now use eq. (6.4) to find both $N_{^8\text{Li,tot}}$ and $N_{\alpha t,\text{tot}}$, and thereby use eq. (6.1) to find the branching ratios this data gives us.

Chapter 7

Results

We now have a way to find how much ^{8}He that reached the carbon foil. Furthermore, we have identified some possible αt-coincidences in the data. This means that we can now use eq. (6.1) to find the branching ratios for the 0° and the 180° coincidences. In table 7.1 we can see the found branching ratios for both categories. In total this gives us a branching ratio of $(0.174 \pm 0.023)\%$ for all the αt-coincidences. The errors on the number of αt-coincidences has been found by assuming that the background from random coincidences is constant at all times, and then determining the background from the data where there is only background, as we marked on fig. 6.5. The errors on the branching ratios has been found with the error propagation equation [38].

Coincidence type	N	N_{eff}	BR [%]
0°	92288 ± 1292	$(4.2 \pm 0.081) \cdot 10^7$	0.12 ± 0.0023
180°	30226 ± 809	$(2.2 \pm 0.062) \cdot 10^7$	0.054 ± 0.0016

Table 7.1: Results from the data analysis presented in chapter 6. N is the measured number of coincidences, N_{eff} is the efficiency corrected number of coincidences and BR is the branching ratio calculated with eq. (6.1).

Chapter 8

Discussion

In chapter 6 I presented the analysis methods that I used during my work of this thesis and in chapter 7 I presented the results from that work. In this chapter I will discuss these methods and results while I attempt to propose further work to be done.

8.1 Evidence for αt-Coincidences

In chapter 6 we found that there were evidence for αt-coincidences in the 0° and 180° coincidence categories. We did however not find a half-life of our data that matched the tabulated value of 119.1 ms. For the 0° coincidences we found a half-life of (212 ± 3.68) ms and for the 180° coincidences we found a half-life of (173 ± 3.62) ms. I did however still conclude that the data primarily contained αt-coincidences. I did this for the following reasons:

1. In section 6.1 we saw that we were not able to remove all the random $\alpha\alpha$-coincidences but only reduce them. This means that we will have some random $\alpha\alpha$-coincidences in our data. As we could see in table 7.1 this random background only constituted a few percent of the measured particles, but it is there.

2. For the 180° data we have seen that it is close to impossible to remove all the time correlated $\alpha\alpha$-coincidences if we do not want to remove all of the data on the diagonal. I tried to remove as many of them as possible by only looking at data with $\theta < 130°$, but it is possible we still had a small background of time correlated $\alpha\alpha$-coincidences. It can be hard to determine how big this background is, as we do not have a way to distinguish between a single $\alpha\alpha$-coincidence and a single αt-coincidence without using the data from the Clovers or the INDiE.

3. We have seen that the half-life of ^{8}Li is 839.9 ms [31], meaning that any data from either random or time correlated $\alpha\alpha$-coincidences will bring the measurement of the half-life up. This is therefore an indication that we have primarily found αt-coincidences with a small background of possibly both random and time correlated $\alpha\alpha$-coincidences.

8.2 Inconsistent Observations in 0°

For the 0° coincidences we found αt-coincidences with the arguments mentioned in section 8.1. We did however only see αt-coincidences in 1 out of the 4 DSSDs, which is rather odd. I am not sure that I am able to explain this behavior, but I do have a suggestion to what can have caused it and how to investigate it. In chapter 6 I presented some plots of the absolute time difference between two hits called ΔT. Here we expected there to be a single peak around 0 ns with a constant background. We did however see more peaks throughout the data as we for example saw in fig. 6.5, indicating that not all the strips in the DSSDs measured the same time. This could have been corrected by doing a time calibration in order to make sure all the strips in the DSSDs measured the same time. But this was not done. Instead, I chose only the data around $\Delta T = 0$ ns, meaning that some valid coincidences was removed. These coincidences could potentially come from the other detectors that did not measure any αt-coincidences. This hypothesis is also backed up by the fact that we did not measure that many coincidences at all in the other detectors, indicating that we may only have been looking at the T_p distribution for the random $\alpha\alpha$-coincidences, as we would only expect few of these. For future work I would therefore suggest that this is investigated further. This can be done by either looking at the other peaks in the ΔT spectrum, and see if they consist of data from the other DSSDs or by making a time calibration and see if the behavior has changed.

8.3 Discussion of the Found Branching Ratios

In table 7.1 I could present the branching ratios for the 180° and the 0° αt-coincidences. These branching ratios were found to be $(0.054 \pm 0.0016)\%$ and $(0.12 \pm 0.023)\%$ respectively. This is $(0.174 \pm 0.023)\%$ in total. In fig. 1.1 and in [7] it is expected that the total branching ratio of all decays to the 9.67 state in ^{8}Li is around 1%. This indicates that a total branching ratio of 0.174% is in good agreement with former research, as we cannot see events with $\theta \geq 130°$. Therefore, we can consider the branching ratio of 0.174% to be a lower boundary of the branching ratio of the decay in eq. (1.2), as I did not get a chance to look for αt-coincidences in the 180° coincidence data in $\theta \geq 130°$.

We have now talked about the possible errors when it comes to finding the total number of αt-coincidences, $N_{\alpha t,\text{tot}}$, in eq. (6.1). We have however not discussed the possible errors on the value of the total number of ^{8}He reaching the carbon foil, $N_{^8\text{He}}$, in the same equation. We will discuss these possible errors here. In section 6.4.1 we found $N_{^8\text{He}}$ by first finding the efficiency corrected number of $\alpha\alpha$-decays from ^{8}Li. This means that we would need to count as many of the $\alpha\alpha$-coincidences as possible to get the correct amount. In section 6.2 we determined that time correlated coincidences with $\theta \geq 130°$ and energies with $|E_1 - E_2| < 500$ keV would be the number of detected $\alpha\alpha$-coincidences from ^{8}Li. We do however not know if there are any αt-coincidences in this data, and if there are, how many coincidences they account for, as mentioned in section 8.1. Furthermore we have sorted away any $\alpha\alpha$-coincidences with angles $< 130°$. There has not been many of these coincidences as the half-life found in the αt-coincidence analysis of 916.6 ± 1.002 ms indicated,

so I do not expect this factor to have had a big impact on $N_{^8\mathrm{He}}$. Furthermore we have not taken the diffused ^{8}He from the 90° coincidence analysis into consideration, but as we saw in section 6.3 these coincidences only made up 0.13% of the total amount of $\alpha\alpha$-coincidences. To summarize I expect that we have taken most of the $\alpha\alpha$-coincidences into consideration.

What could have also had an impact on $N_{^8\mathrm{He}}$ is the branching ratio from ^{8}He to the first excited state of ^{8}Li. This branching ratio is set to be 84% as it was also shown on fig. 1.1. This value has only been measured once in [8]. It has never been reproduced in any of the following research.

We will also have to discuss the uncertainties on the branching ratios presented in chapter 7. As it was mentioned, the uncertainties on the number of both $\alpha\alpha$-decays and on αt-decays, was found by assuming that the number of random $\alpha\alpha$-coincidences was the only source of background. But as we have already discussed, we cannot directly distinguish $\alpha\alpha$-coincidences from αt-coincidences, meaning that we do not know if the only background we had came from random $\alpha\alpha$-coincidences or if it also came from time correlated $\alpha\alpha$-coincidences. What we can say is however that the closer to the tabulated value of the half-life of ^{8}He we can get with our data, the less background we would expect to have. Therefore, it seems that we still have a small background from ^{8}Li, but as the measured half-lives of our data was much closer to the half-life of ^{8}He than ^{8}Li this background is not dominant. If we want to get an idea of how much ^{8}Li we have in our αt-coincidence data, a new fit to the T_p spectra could be made where we allow a component from the decay of ^{8}Li to two α-particles to be part of the fit. From the front factors of this fit we could thereby get an idea of how much ^{8}Li we would expect to have measured.

8.3.1 Suggestion to get Better Branching Ratios in Future Work

If we want to successfully look for more αt-coincidences in the 180° coincidence data, we need a way to be able to remove as many $\alpha\alpha$-coincidences from the decay of ^{8}Li as possible. When we are only looking at data from the DSSDs and plastics we are restricted in our possibilities, as we do not have any way to distinguish an $\alpha\alpha$-coincidence from an αt-coincidence, when they are placed in the same range of energy. We could in theory use the T_p spectrum to sort away data with T_p values higher than maybe 5 or 10 half-lives of ^{8}He, as the half-life of ^{8}Li is much larger. This would greatly reduce the amount of $\alpha\alpha$-coincidences from ^{8}Li, but it would not remove them. This method would not give us a way to determine how big the ratio of αt-coincidences to $\alpha\alpha$-coincidences is either. Again, because we cannot directly distinguish these particles from each other by only doing a DSSD measurement. Furthermore we have used the T_p spectrum to validate whether we have found αt-coincidences or not. With this method we cannot do this anymore, as the T_p spectrum has already been used to remove $\alpha\alpha$-coincidences, hence we cannot use it again as a validation.

To get more information about αt-coincidences in the 180° detectors we therefore have too look somewhere else. This can be done looking for αtn-coincidences by

including the neutron detections from the INDiE neutron detector in the analysis as well. We know that the $\alpha\alpha$-coincidences from the decay of ^{8}Li will not have any other particles in their decay, meaning that we will not expect to measure a coincidental neutron in the INDiE for these decays. If we measure a coincidental neutron in the INDiE, we will therefore have a way of confirming that we have measured an αt-coincidence in the DSSDs, and we do therefore not need to do any sorting by the relative angle between the 2 detections. I would therefore suggest that an αtn-coincidence analysis will be made if further work is to be done on this experiment.

8.4 Discussion of the 90° Coincidence Data

We have now been discussing the success of finding αt-coincidences in 0° and 180°. We did however not find any αt-coincidences in the 90° coincidence data. This in itself is a nice result, but I was not able to determine what the data actually was. If we looked at the data from the ΔT-spectrum in fig. 6.14, we first of all saw that the tallest peak does not lie closest to 0 ns. This indicates a potential problem by not doing a time calibration for all detector strips, as we lost a lot of information from the data by removing it. We did for the 90° coincidence data look in a bigger time window than for the other data. This have potentially caused us to have a slight increase in the background of 90° data. Speaking of background, we can see that we have a relatively small, but not insignificant, background of random coincidences in the 90° data. All of this information gives us a couple of options to explain the data we see, and I will here list some of my observations:

1. We can from the data be sure that we do not have a clear spectrum of αt-coincidences, as the half-life of (707 ± 6.37) ms is not close to the half-life of ^{8}He.

2. We may measure a clear spectrum of coincidental $\alpha\alpha$-decays from ^{8}Li, as the half-life of the data is close to, but not the same as the half-life of ^{8}Li. This does not make sense, as we have already the removed ^{8}He that diffused out of the target as explained in section 6.3.1.

3. We do not have a set of data with completely random non-time correlated $\alpha\alpha$-coincidences, as we could else expect. First of all because we would have seen a bigger background in the ΔT spectrum, but also as we would have expected to measure a half-life of around half the half-life of ^{8}Li as I explained in section 4.3.

4. Looking at fig. 6.12 we can see that many of the coincidences we have left after the removal of the diagonal seems to have the spectrum of a single α from the decay of ^{8}Li combined with something of a low energy. I have tried to see if these low-energy particles could be electrons from the β-decay of ^{8}He with the method described in fig. 6.3. The energy spectrum of the possible betas was the same as the energy spectrum of the data that was not found to come from a β-decay as we can see on fig. 8.1. This was to be expected from the analysis we did with the decay of ^{20}Na, but it also indicates that it is not electrons we have measured in the detector.

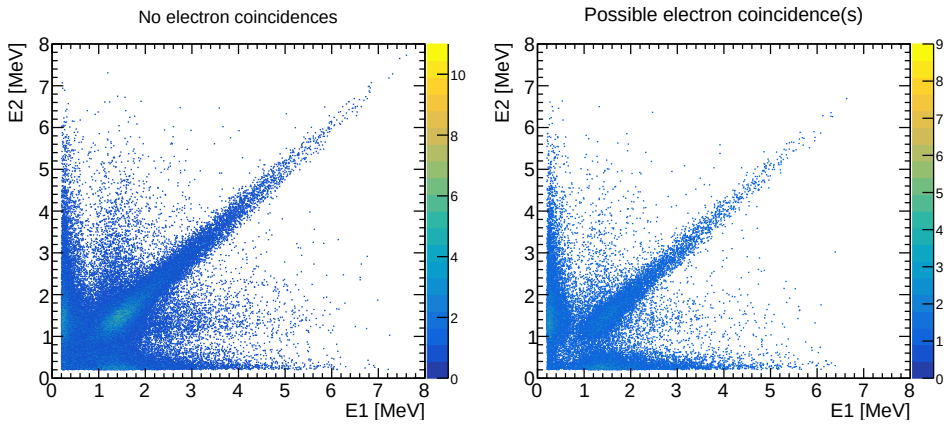

FIGURE 8.1: Energy spectra of the time correlated 90° coincidence data separated in the possible detected electron coincidences and the coincidences that we know has not been coincident with an electron.

From all of this it is therefore not clear what the data in fig. 6.14 is. We can however conclude that it is not αt-coincidences. To me, we have most likely measured the coincidences between an electron and an α from the decay of ^{8}Li, which could indicate that a time calibration of the data is necessary to make my analysis of β-particles valid.

8.5 Further Outlook

As mentioned in chapter 1 the decay from eq. (1.2) is possible from either the 5.40 MeV or the 9.67 MeV state of ^{8}Li. Now that we have found some of the energy distributions of this decay in chapter 6, it would make sense to start analysing these further to find out how much each of these energy levels contribute to the decay. If we want even better information about the decay and the energy levels, I would recommend that we also look at the αtn-coincidences as I have already recommended in this chapter, as we can then use the energies of each particle to sum up their total energies and thereby find the energy, width and possible mixing of the two states.

Chapter 9

Conclusion

I have now been looking at the decay of ^{8}He through the decay channel $^{8}\text{He} \rightarrow {}^{8}\text{Li}^{*} \rightarrow \alpha + \text{t} + \text{n}$. The goal for this thesis was to see how much information we were able to extract from this decay, when we left some of the most time consuming parts of the analysis out: The analysis of αtn-coincidences and the time calibration of the detectors. I did this by only looking for αt-coincidences in the DSSDs. I can conclude that it is possible to find αt-coincidences without these methods, as I was able to find αt-coincidences in detectors placed 0° and 180° from each other with a branching ratio of $(0.12 \pm 0.0023)\%$ and $(0.054 \pm 0.0016)\%$ respectively. In total we get a branching ratio of $(0.174 \pm 0.0023)\%$. But as we have possibly removed a lot of αt-coincidences in order to remove the background of $\alpha\alpha$-coincidences this number can only be regarded as a lower boundary. Therefore, I would recommend to include the data from the INDiE to look for αtn-coincidences to get a more precise value of this branching ratio. I did not find any αt-coincidences in detectors placed 90° from each other, and it was hard to conclude where the data we saw came from. Therefore, I recommend that time calibrations on all the detectors will be made in order to make sure that all data is correctly compared.

Bibliography

[1] H. Harari. "A new quark model for hadrons". In: *Physics Letters* 57B.3 (1975), p. 265.

[2] M. Kobayashi and T. Maskawa. "CP-Violation in the Renormalizable Theory of Weak Interaction". In: *Progress of Theoretical Physics* 49.2 (1973), p. 652.

[3] S. Chatrchyan et al. "Observation of a new boson at a mass of 125 GeV with the CMS experiment at the LHC". In: *Physics Letters B* 716.1 (2012), pp. 30–61.

[4] P.W. Higgs. "Broken Symmetries and the Masses of Gauge Bosons". In: *Phys. Rev. Lett.* 13 (16 Oct. 1964), pp. 508–509.

[5] W. Rodejohann, X-J. Xu, and C. E. Yaguna. "Distinguishing between Dirac and Majorana neutrinos in the presence of general interactions". In: *Journal of High Energy Physics* 5 (May 2017), p. 24.

[6] F. P. An et al. "Precision Measurement of Reactor Antineutrino Oscillation at Kilometer-Scale Baselines by Daya Bay". In: *Phys. Rev. Lett.* 130 (16 Apr. 2023), p. 161802.

[7] C. Jollet and A. Meregaglia. "9Li and 8He decays in GEANT4". In: *Nuclear Instruments and Methods in Physics Research Section A: Accelerators, Spectrometers, Detectors and Associated Equipment* 949 (2020), p. 162904.

[8] T. Björnstad et al. "The decay of 8He". In: *Nuclear Physics A* 366.3 (1981), pp. 461–468.

[9] M.J.G. Borge et al. "Beta-delayed triton emission in the decay of 8He". In: *Nuclear Physics A* 460.3 (1986), pp. 373–380.

[10] M.J.G. Borge et al. "Study of charged particles emitted in the β-decay of 6,8He". In: *Nuclear Physics A* 560.2 (1993), pp. 664–676.

[11] F.C. Barker and E.K. Warburton. "The beta-decay of 8He". In: *Nuclear Physics A* 487.2 (1988), pp. 269–278.

[12] F.C. Barker. "The 8He delayed triton spectrum and β-decay to unstable levels". In: *Nuclear Physics A* 609.1 (1996), pp. 38–42.

[13] E. Vogt. *R-Matrix Theory*. Lecture notes. 2004.

[14] V. Zelevinsky and A. Volya. *Physics of Atomic Nuclei*. Boschstr. 12, 69469 Weinheim, Germany: Wiley-VCH, 2017.

[15] B.R. Martin and G. Shaw. *Nuclear and Particle Physics*. 3rd ed. Wiley, 2019.

[16] Jerzy Cetnar. "General solution of Bateman equations for nuclear transmutations". In: *Annals of Nuclear Energy* 33.7 (2006), pp. 640–645.

[17] K. Riisager. *Nuclear Physics II, spring 2022 – Notes*. Jan. 2022.

[18] D.H. Perkins. *Introduction to High Energy Physics*. 4th ed. Cambridge University Press, 2000.

[19] E. Lopienska. *The CERN accelerator complex, layout in 2022. Complexe des accélérateurs du CERN en janvier 2022*. General Photo. 2022. URL: http://cds.cern.ch/record/2800984 (visited on 05/18/2023).

[20] A. Herlert. "High-statistics measurement of the β-delayed αspectrum of 20Na". In: *Nuclear Physics News International* 20.4 (2010), p. 5.

[21] B. Jonson and K. Riisager. *The ISOLDE facility*. URL: http://www.scholarpedia.org/article/The_ISOLDE_facility (visited on 04/13/2023).

[22] ISOLDE Yields Database. *Yield details*. URL: https://isoyields2.web.cern.ch/YieldById.aspx?Yield_Id=352 (visited on 04/13/2023).

[23] U. Bergmann. "Exotic Decays of Nuclei at the Limits of Existence". PhD thesis. Aarhus University, 2000.

[24] *Targets and Separators*. URL: https://isolde.cern/targets-and-separators (visited on 05/23/2023).

[25] H. Geissel, G. Munzenberg, and K. Riisager. "Secondary Exotic Nuclear Beams". In: *Annual Review of Nuclear and Particle Science* 45.1 (1995), pp. 163–203.

[26] S.N. Ahmed. *Physics & Engineering of Radiation Detection*. 2nd ed. Elsevier, 2015.

[27] S.L. Johansen. "A study of the β^- response of silicon detectors and the effects of backscattering in a complex setup using GEANT4". MSc Thesis. Aarhus Univeristy, June 2021.

[28] Aarhus Subatomic Group. *Energy Loss Calculator*. URL: https://eloss.kern.phys.au.dk/ (visited on 04/04/2023).

[29] G.F. Knoll. *Radiation Detection and Measurement*. 3rd ed. John Wiley & Sons, 2000.

[30] C. Rahbek. "Radiative Transitions in ^{8}Be using the ^{7}Li(p,γ)$\alpha\alpha$ reaction". B.S. Thesis. Aarhus Univeristy, June 2021.

[31] National Nuclear Data Center. *Evaluated Nuclear Structure Data File*. URL: https://www.nndc.bnl.gov/ensdf/ (visited on 01/18/2023).

[32] Aarhus Subatomic Group. *AUSAlib*. URL: https://gitlab.au.dk/ausa/ausalib (visited on 05/22/2023).

[33] K.L. Laursen et al. "High-statistics measurement of the β-delayed αspectrum of 20Na". In: *The European Physical Journal A* 49.6 (2013), p. 79.

[34] J. Halkjær. *AUSAlib tutorial*. URL: `https://gitlab.au.dk/ausa/ausalib/-/wikis/tutorial` (visited on 04/03/2023).

[35] Aarhus University Subatomic Group. Private communication. 2023.

[36] E.A.M. Jensen. *Solid Angle Matrix*. URL: `https://gitlab.au.dk/ausa/erik/solidanglematrix` (visited on 05/17/2023).

[37] H.O.U. Fynbo. "Beta-delayed particle emission from the dripline nuclei ^{11}Li, ^{31}Ar and ^{9}C". PhD thesis. Aarhus University, 1999.

[38] P.R. Bevington and D.K. Robinson. *Data Reduction and Error Analysis for the Physical Sciences*. 3rd ed. McGraw-Hill, 2003.